

Dynamical Landscape and Multistability of the Earth's Climate

Georgios Margazoglou and Valerio Lucarini*

*Department of Mathematics and Statistics, University of Reading, Reading, United Kingdom and
Centre for the Mathematics of Planet Earth, University of Reading, Reading, United Kingdom*

Tobias Grafke

Mathematics Institute, University of Warwick, United Kingdom

Alessandro Laio

International School for Advanced Studies (SISSA), Trieste, Italy

(Dated: May 17, 2023)

We apply two independent data analysis methodologies to locate stable climate states in an intermediate complexity climate model. First, drawing from the theory of quasipotentials, and viewing the state space as an energy landscape with valleys and mountain ridges, we infer the relative likelihood of the identified multistable climate states, and investigate the most likely transition trajectories as well as the expected transition times between them. Second, harnessing techniques from data science, specifically manifold learning, we characterize the data landscape of the simulation data to find climate states and basin boundaries within a fully agnostic and unsupervised framework. Both approaches show remarkable agreement, and reveal, apart from the well known warm and snowball earth states, a third intermediate stable state in one of the two climate models we consider. The combination of our approaches allows to identify how the negative feedback of ocean heat transport and entropy production via the hydrological cycle drastically change the topography of the dynamical landscape of Earth's climate.

Keywords: Climate modelling, multistability, transitions, instantons, quasipotential theory, nonequilibrium systems, data-driven methods, manifold learning

I. INTRODUCTION

The climate, an extremely high-dimensional complex system, is composed of five interacting subdomains: a gaseous atmosphere, a hydrosphere (water in liquid form), a lithosphere (upper solid layer), a cryosphere (water in solid form) and a biosphere (ecosystems and living organisms) [1]. The climate is driven by the (inhomogeneous absorption of) incoming solar radiation and can be treated as a highly non-trivial dynamical system that features spatio-temporal variability on a vast range of scales. The system is at an approximate nonequilibrium steady state (except when exhibiting critical transitions) due to the resulting interplay of forcings, dissipation, positive and negative feedbacks, instabilities and saturation mechanisms [2]. The presence of periodic as well as irregular fluctuations in the boundary conditions do not allow the climate to reach an exact steady state [3, 4].

A straightforward attempt to mathematically formulate the dynamics of the climate system is by defining a set of partial differential equations (PDEs) that govern the evolution of the field variables (e.g. velocity \mathbf{v} , temperature T , pressure p , density ρ , concentration of various chemical species) in a rotating (3+1) spacetime domain and describe the budget of mass, momentum and energy. As this set of PDEs is impossible to solve analytically, they are usually simulated numerically. Depending

on the number of resolved variables, this procedure is extremely challenging both from a technological and scientific point of view, and requires a diversified approach. Indeed, one needs climate models that vary in complexity, flexibility, purpose and computational cost. Therefore, a hierarchy of climate models can be established [5–8]. At the lowest level of such a hierarchy one can find simple zero or one-dimensional Energy Budget Models (EBMs) that model the energy exchange in the atmosphere or triggered by the solar radiation [9–11], as well as low-dimensional models that represent fundamental processes of the large scale oceanic [12–14] and atmospheric dynamics [15–17]. Next come the so-called intermediate complexity models, which provide a parsimonious yet Earth-like representations of the dynamics of climate, see e.g. [18–21]. Finally, modern state-of-the-art climate models, similar to the ones featured in the latest Intergovernmental Panel on Climate Change (IPCC) report [22] are based on applying a series of necessary truncations and approximations in such a set of PDEs. They simulate, using massive high performance computing resources, a representative amount of physical, chemical, and biological processes of the climate system and attempt to explore its past, present, and future [4, 23]. Additionally, the impact of the neglected scales of motions on the explicitly resolved scales is approximated via suitably developed parametrizations, which include deterministic, stochastic, and possibly non-Markovian components [24].

* Corresponding author. Email: v.lucarini@reading.ac.uk

A. Global Stability Properties of the Climate System

The climate system features multistability both globally and locally, and is characterized by critical transitions among stable states. Such transitions are often termed tipping points in the geophysical community. Examples of geographically localized phenomena affecting the climate system featuring such a behaviour – the so-called tipping elements [25] – include the dieback of the Amazon forest [26], the shut-down of the thermohaline circulation of the Atlantic ocean [27], the methane release resulting from the melting of the permafrost [28], and the collapse of the atmospheric circulation regime associated to the Indian monsoon [29]; all of which can be seen as local features of multistability. A critical transition taking place for one climatic subsystem may trigger the tipping of another element: this is the phenomenon of so-called cascading tipping points [30, 31].

However, when considering the Earth system macroscopically as a whole, a remarkable example of a radical critical transition can be found among at least two possible steady climatic states [9–11]. Indeed, the current astronomical configuration of Earth supports the present day Warm (W) climate, and a frozen one, termed Snowball (SB), which exhibits global glaciation, extremely low temperatures and limited climatic variability [32, 33]. Geological and paleomagnetic evidence suggests that during the Neoproterozoic era (in particular around 630 and 715 million years ago), the Earth exhibited at least two major long lasting global glaciation periods, thus entering twice into the snowball climate state [34, 35]. Similarly, numerical models of exoplanets suggest the existence of many more stable climates depending on the precise parameters, such as for example 5 co-existing climate regimes on aquaplanets [36].

In this work we bring forward the scientific programme proposed in [4]. In particular, we explore the multistable phase space of Earth’s climate system through methods from nonequilibrium statistical physics, dynamical systems, and data science. Concretely, following on the perspective indicated in the Appendix of [37] and related to the debate revolving around the relevance of the theory of punctuated equilibrium for evolution [38, 39], we propose a holistic view of climate as a stochastic motion in a nonequilibrium potential landscape, similar in spirit to Waddington’s “epigenetic landscape” metaphor in evolutionary biology [40–43]. In our case, the macroscopic climate states are represented by vast valleys in this landscape, which are explored over long timescales and only rarely transitioned out of into neighboring valleys. Within it there are smaller scale features in which the system can get stuck for shorter times, such as the tipping points mentioned above, localized both in their geographic extent and temporal permanence. One can imagine a full spectrum of scales for localized valleys, separated by mountain passes (which the system crosses when a transition occurs), ridges, and highlands (in which the

system meanders until finding a nearby valley to descent into). The advantage of this picture, apart from being an intuitive qualitative description, is that it is *non-perturbative* and *global*.

Indeed, the metastable states of the climate system correspond to the local minima of a quasi-potential function Φ , which generalizes the idea of an energy landscape and has both a dynamical and probabilistic meaning, as discussed below. We present in Fig. 1a) a cartoon of what we have in mind, where the possible states of the climate are described by the vector X . The quasi-potential features troughs, saddles, and ridges at different scales and should be interpreted as a high-dimensional object. Applying a deterministic and/or a stochastic forcing makes it possible for the system to explore various regions of Φ .

Let’s make, for clarity of exposition, the simplifying assumption that we consider X as uni-dimensional and we identify it with the globally averaged surface temperature, where the current state of the climate is given by the red dot. Indeed, currently we are in an interglacial period (level 3; Holocene) of an ice-age (level 2; Pleistocene/Quaternary glaciation) taking place during a W climate state (level 1). In this metaphor, the two competing coarse grained states differ by $O(100)$ K at level 1; by $O(10)$ K at level 2; by $O(1)$ K at level 3. The intensity of noise allowing for exploring transitions between competing states decreases dramatically as we go from level 1 to level 3, because the local minima become shallower. Going to even smaller scales, one would find additional (shallower) corrugations of Φ , corresponding to the regional tipping points mentioned above. Multistability in the climate system is often revealed by the presence of hysteresis loops obtained when suitable parameters of the system are changed, usually quasi-adiabatically [27, 32, 44]. Figure 1b) shows schematically how the multistability portrayed in Fig. 1a) appears when applying suitable protocols of parametric modulations to the system.

Climate models face unavoidable limitations due to the fact that they cannot represent explicitly all processes occurring in the Earth system nor are able to resolve all scales of motion: cutoffs are present both on the very fast and/or the very slow components. As a result, some of the qualitative features of multistability will be lost, thus limiting the realism and range of applicability of a given model [6].

B. Outline of the Paper and Main Results

Response theory allows to reconstruct locally in the parameters’ space the impacts on climate of perturbations to its dynamics [2, 45]. When applied in the context of time-dependent perturbations of moderate intensity, response theory is key to reconstructing the pullback attractor on which the time-dependent measure of the system is supported [4, 46]. Nonetheless, the applicability of response theory is inherently limited, as the radius of

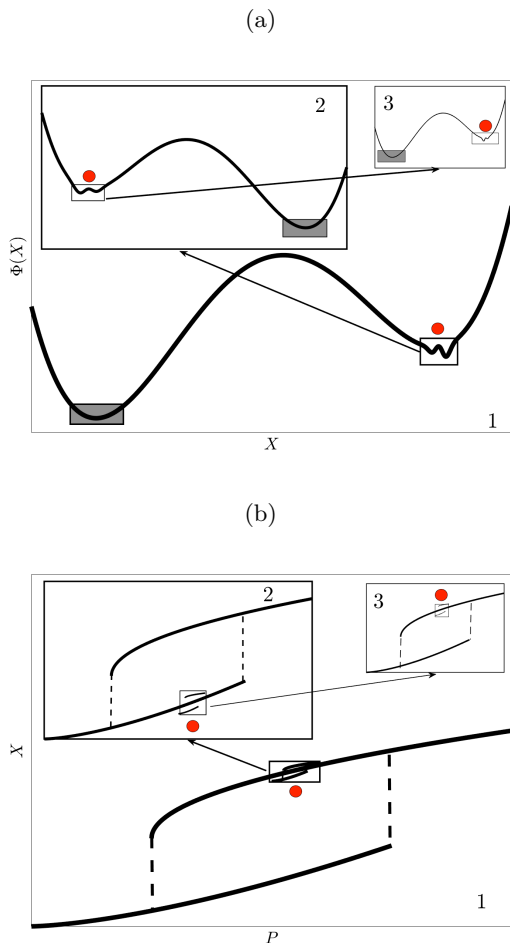


FIG. 1. Schematic representation of the multiscale nature of multistability in the climate system. a) Quasipotential Φ as a function of X , where X is a representative coordinate describing the state of the system. b) Corresponding hysteresis loops as a function of a parameter P . The white boxes indicate the zoomed-in current state of the system (red dot), going from 1 to 3 towards smaller and smaller scales. See text for details.

expansion of this perturbative approach is, by and large, proportional to the spectral gap of the transfer operator of the unperturbed system [47, 48]. Response theory breaks down, by definition, near critical transitions, where the spectral gap is vanishing and the decay of the correlations becomes very slow [49, 50].

In this paper we will focus on global properties of the climate system and study the transitions between competing attractors. We will see how this allows us to reason about the relative probability of the respective climate states, as well as about the expected times and pathways for transitions between them. Unfortunately, we will mostly be able to study multistability only at the largest scale, as indicated with 1 in Fig. 1. Indeed, as discussed below, in order to explore the landscape of metastable state, we will force the climate by adding stochastic forcing. However, the intensity of the forcing needed to study

effectively the large scale metastability is too strong for retaining the features of the smaller scale ones, which are washed out by noise. In one case we will need to resort to using much smaller noise intensities for studying selectively the decay from a shallow metastable state. This is an example of the beauty and of the curse of multiscale systems: dedicated modelling exercises must usually focus on only one scale of interest, unless one is able to use wisely some form of learning and targeted optimization procedures.

In order to obtain data to analyse from this novel perspective, we employ PLASIM [51], a simplified climate model that has shown extreme flexibility in describing the dynamics of a vast range of climate conditions, including very exotic ones [46, 52–56]. The model features $O(10^5)$ degrees of freedom (d.o.f.). We consider two setups of the model – one allowing for the ocean to transport heat from low to high latitudes (setup A), previously used in [46], and one where only the atmosphere is able to perform large scale heat transport (setup B), previously used in [55].

In this case, we force the model by allowing the solar irradiance S^* to randomly fluctuate around the present-day mean value of $S^* = 1365 \text{ W/m}^2$, thus triggering transitions among the competing climate states. Along the lines of [37, 57], we aim at studying the invariant measure and the statistics of the noise induced transitions among attractors by constructing the quasipotential of the stochastically perturbed system [58–61]. Such a function, with the caveats discussed below, defines an effective energy landscape for the climate model and is key to understanding the properties of the invariant measure of the system and of the noise-induced transitions. We compute the transitions paths among attractors composed of instantonic and relaxation trajectories by averaging over many transition events.

The identification of the competing attractors is approached in two ways. First, we use standard forward numerical modelling and identify different asymptotic states, associated with separate basins of attraction, when stochastic forcing is removed from the system. Second, competing attractors are automatically detected through data-driven methods applied to the output of long stochastic integrations of the model. Such methods have been used for studying metastable states in biomolecules, and allow one to reconstruct very effectively the quasi-potential Φ of the system, partially taking care of the *curse of dimensionality*, and to identify its local minima and saddles [62–65].

As an additional diagnostic tool, inspired by [50, 66], we construct a finite state Markov chain representation of the transfer operator [67] of the system in a reduced phase space composed of the global surface temperature and the Equator to Poles temperature difference and use it to compute and interpret the slow modes of variability of the system in terms of intra- and inter-well dynamics.

We anticipate that whereas in setup A we find the two usual W and SB states, we surprisingly discover that

setup B features the presence of a third stable climate state (to be termed “cold climate” (C) in the following), with an ice free latitudinal band at about $\pm 20^\circ$ around the Equator and mild, larger than 10°C surface temperatures, along with vigorous atmospheric circulation and non-trivial hydrological cycle in the same band. Such a third state resembles previously discovered exotic climatic configurations such as the slushball Earth [68] and the Jormungand state [69]. Furthermore, it corresponds to a shallow minimum of the quasipotential and disappears when ocean transport, which acts as a strong stabilizing mechanism, is introduced in the system.

The paper is structured as follows. Section II contains the mathematical framework behind our analysis. Section III provides a description of the climate model used in this study. Section IV contains the description and critical analysis of the obtained results. Section V is dedicated to drawing the conclusion of this work and to presenting future research perspectives. The supplementary material (SM) attached to this paper as Appendix contains some extra information on the computation of the average transition paths and a brief and informal description of the mathematics of the transfer operator and of its finite-size representation. Additionally, it allows the reader to enjoy informative and hopefully aesthetically pleasing movies related to the numerical simulations performed in this study

II. QUALITATIVE AND QUANTITATIVE ASPECTS OF THE MULTISTABILITY OF THE CLIMATE SYSTEM

A. Dynamical Landscape of the Climate System

As mentioned above, the dynamics of the geophysical fields is described by PDEs. Nonetheless, we approach the study of global climate and its multistable character from the perspective of finite dimensional dynamical systems. In fact, EBMs provide an extremely coarse grained yet very informative description of the main energy exchanges in the climate system [6]. In its simplest form the tendency of energy budget is modeled by the difference between the incoming and outgoing radiation

$$C \frac{dT}{dt} = I(1 - \alpha(T)) - O(T) \rightarrow \frac{dT}{dt} = -\frac{d}{dT} \Phi(T), \quad (1)$$

where effectively the Earth is reduced to a 0-dimensional system, with the global temperature T being the only degree of freedom. Here, t is time, $I = S^*/4$ is the average incoming solar radiation per unit area, C is an effective average heat capacity per unit area, and $\alpha \in [0, 1]$ is the albedo. α depends on T , with low (high) T resulting in high (low) α , which causes the positive ice-albedo feedback, i.e. ice reflects efficiently the solar radiation. $O(T)$ is a monotonically increasing function of T and models the outgoing radiation per unit area. In other words, a

warmer surface emits more radiation, which is the principle behind the Boltzmann (negative) radiative feedback. The interplay between these two competing mechanisms results in a bistable climate, where Earth asymptotically approaches the W or the SB state. In Eq. (1) we can define a potential $\Phi(T)$, which has two minima corresponding to the W and SB states, together with an unstable local maximum between the two.

A multidimensional deterministic dynamical system can be defined as a set of ordinary differential equations

$$\frac{d\mathbf{x}}{dt} = \mathbf{F}(\mathbf{x}, t), \quad \mathbf{x}_0 \equiv \mathbf{x}(t=0), \quad (2)$$

where $\mathbf{x}(t) \in \mathbb{R}^N$ describes the state of the system at time t with initial condition \mathbf{x}_0 , and $\mathbf{F}(\mathbf{x}, t) \in \mathbb{R}^N$ is a smooth vector field. The initial condition \mathbf{x}_0 determines the asymptotic state of its orbit. If Eq. (2) possesses more than one asymptotic states, defined by the attractors Ω_j , $j = 1, \dots, J$, the system is multistable. The phase space is partitioned between the basins of attraction B_j of the attractors Ω_j and the boundaries ∂B_l , $l = 1, \dots, L$ separating such basins, which possess a set of saddle points Π_l , $l = 1, \dots, L$. Such saddle points attract initial conditions on the basin boundaries [70–72] and can be computed using the so-called edge tracking algorithm [73], which was used in an EBM by [74]. Chaotic unstable saddle, then termed Melancholia (M) states, have been constructed with the edge tracking algorithm for a simplified climate model built by coupling a primitive equation atmosphere with a diffusive ocean [33].

Escaping an attractor is only possible if the system is forced by a properly defined external deterministic forcing or perturbed by a stochastic noise. The theory of tipping points has been recently extended to deal with all of these scenarios [75]. In particular, noise-induced escapes from attractors have long been studied in natural sciences [76, 77] and have, in parallel, inspired extremely fruitful mathematical investigations [78]. By subjecting Eq. (2) to a Gaussian random noise and considering it in Itô form, we write the stochastic differential equation

$$d\mathbf{x} = \mathbf{F}(\mathbf{x})dt + \sigma \mathbf{s}(\mathbf{x})d\mathbf{W}, \quad (3)$$

where $d\mathbf{W}$ is the increment of an M -dimensional Wiener process, $\mathbf{F}(\mathbf{x})$ is in this context usually referred to as the drift term, $\mathbf{C}(\mathbf{x}) = \mathbf{s}(\mathbf{x})\mathbf{s}(\mathbf{x})^T \in \mathbb{R}^{N \times N}$ is the noise covariance matrix where in general the volatility matrix $\mathbf{s}(\mathbf{x}) \in \mathbb{R}^{N \times M}$, and $\sigma \geq 0$ determines the strength of the noise.

The use of stochastic dynamical systems for studying the climate has a long history and has been key to understanding at fundamental level the relationship between climate response to perturbations and climate variability [3, 4, 6, 79–81]. In the present work, introducing stochasticity in the form a yearly fluctuating solar constant, there is only one independent Brownian motion, so that $\mathbf{s}(\mathbf{x}) \in \mathbb{R}^{N \times 1}$ and $\mathbf{C}(\mathbf{x})$ is rank one. Additionally, only the d.o.f. directly associated to the incoming

solar radiation are directly impacted by the stochastic forcing. We are extremely far from elliptic diffusion processes, where all d.o.f.'s of the system undergo random forcing. As clarified in [37] and motivated by the way the climate energy exchange processes work, we expect that the applied noise percolates to all d.o.f.'s of the system as a result of non-degenerate interplay between stochastic forcing and the deterministic component of the dynamics given by the drift term, so that we can assume that we are dealing with a hypoelliptic diffusion process [82]. As a result, we expect that for all values of $\sigma > 0$ the invariant measure of the system is smooth.

The contributions by [59–61, 83] extend the classic Freidlin-Wentzell's theory [78] and allow for studying stochastic processes in nonequilibrium systems featuring multiple deterministic attractors in the form of Eq. (3). In particular, in the limit $\sigma \rightarrow 0$, they introduce the quasipotential $\Phi(\mathbf{x})$, a nonequilibrium generalization of the notion of free energy, which intuitively characterizes the log-likelihood of reaching a point \mathbf{x} . With this, the invariant measure can be written as a large deviation law

$$\rho_\sigma(\mathbf{x}) \sim Z(\mathbf{x}) \exp\left(-\frac{2\Phi(\mathbf{x})}{\sigma^2}\right), \quad (4)$$

where $Z(\mathbf{x})$ is a field depended pre-exponential factor. By studying a small- σ asymptotic expansion of the invariant measure of the system obtained as stationary solution to the Fokker-Planck equation (see Eq. (1) in Sec. III of the Supplementary Material and subsequent discussion) Eq. (3), one obtains the following Hamilton-Jacobi equation [60, 84]:

$$F_i(\mathbf{x})\partial_i\Phi(\mathbf{x}) + C_{ij}(\mathbf{x})\partial_i\Phi(\mathbf{x})\partial_j\Phi(\mathbf{x}) = 0. \quad (5)$$

This equation allows one to express Φ in terms of the drift and volatility fields introduced in Eq. (3). The quasipotential Φ can also be computed by solving the variational problem associated with the Freidlin-Wentzell action [85].

The function Φ is key to understanding the properties of the system. Indeed, it is possible to write the drift vector field as the sum of two vector fields:

$$F_i(\mathbf{x}) = R_i(\mathbf{x}) - C_{ij}(\mathbf{x})\partial_j\Phi(\mathbf{x}) \quad (6)$$

that are mutually orthogonal, so that $R_i(\mathbf{x})\partial_i\Phi(\mathbf{x}) = 0$. In the case Eq. (3) describes a thermodynamical system near equilibrium, \mathbf{R} defines the time reversible dynamics, while $\mathbf{F} - \mathbf{R}$ defines the irreversible, dissipative dynamics [58]. A different strategy for attaining the decomposition of the drift term into a symmetric and an antisymmetric component has been proposed by [86, 87].

Additionally, Φ is a Lyapunov function whose decrease describes the convergence of an orbit to the attractor. Specifically, $\Phi(\mathbf{x})$ has local minima at the deterministic attractors Ω_j , $j = 1, \dots, J$, and has a saddle behaviour at the saddles Π_l , $l = 1, \dots, L$. If an attractor (saddle) is chaotic, Φ has constant value over its support, which can then be a strange set [59, 83].

A special class of trajectories, named instantons, define, in the zero-noise limit, the most probable way to exit an attractor [77, 88]. An instanton connects an attractor Ω to a point \mathbf{x} within the same basin of attraction and can be obtained by minimizing the action of the stochastic field theory associated with the system [85, 89, 90]. The instanton is intimately connected to the quasipotential $\Phi(\mathbf{x})$ in that the local quasipotential $\Phi_\Omega(\mathbf{x})$ within the basin of attraction of Ω is equal to the action for the instanton between Ω and \mathbf{x} . The instantonic trajectory obeys the equation of motion $dx_i/dt = R_i(\mathbf{x}) + C_{ij}(\mathbf{x})\partial_j\Phi_\Omega(\mathbf{x})$, which has a reversed component of the gradient contribution with respect to the drift field, see Eq. (6). To recover the global quasipotential $\Phi(\mathbf{x})$, one needs to resort to a pruning-and-stitching strategy, glueing together the local portions Φ_{Ω_j} , $j = 1, \dots, J$, see [83] and the careful description recently provided by [61]. A separate view on this problem, based upon a different interpretation of the noise has been proposed in [86, 87].

Instantonic trajectories allow to reason about expected escape times in the zero-noise limit. Escapes from an attractor Ω through a saddle Π into a neighbouring basin are Poisson-distributed events, where the probability that an orbit does not transition up to time t is, similarly to the classic Kramers' law [91], given by:

$$P(t) = \frac{1}{\bar{\tau}_\sigma} \exp\left(-\frac{t}{\bar{\tau}_\sigma}\right), \text{ with } \bar{\tau}_\sigma \propto \exp\left(\frac{2\Delta\Phi_{\Omega \rightarrow \Pi}}{\sigma^2}\right), \quad (7)$$

being the expected escape time and $\Delta\Phi_{\Omega \rightarrow \Pi} = \Phi_\Omega(\Pi) - \Phi_\Omega(\Omega)$ is the quasipotential barrier height at the relevant saddle [72]. Unfortunately, due to the global stitching procedure, one cannot in general simply read off the barrier height $\Delta\Phi_{\Omega \rightarrow \Pi}$ from the $\Phi(\mathbf{x})$ of equation (4). While the global quasipotential $\Phi(\mathbf{x})$ yields information about the relative probability of attractors, and is available e.g. through global sampling of the system, the local notion of potential barriers, $\Delta\Phi_{\Omega \rightarrow \Pi}(\mathbf{x})$ is relevant for the time-scale of transition events, and can be obtained e.g. by looking at transition times between attractors. In the case of multistability, the local and global notions of quasipotential can be brought to a common ground if the system is at equilibrium so that no global probability fluxes are present. Equivalence between the information provided by the local and global quasipotentials is also realized if the system is not an equilibrium one but only two competing states are present with a single saddle embedded in the boundary between the two basins of attraction, as in the cases analysed in [37, 57]. In general, we will resort to measuring separately the invariant measure (4) and the barrier heights (7).

B. Exploring the topography of the quasipotential

A key role in our analysis is played by the quasipotential Φ defined in Eq. (4), because, as mentioned above, the topography of Φ determines the macroscopic features

of the dynamics. In general a multiscale landscape will be characterized by a relatively few large basins, separated by high barriers, decorated by smaller local minima like in the example of Fig. 1 .

To study the topography of Φ one can neglect the pre-exponential factor $Z(x)$ in Eq. (4) and project the invariant measure $\rho_\sigma(x)$ on a small number of pre-selected variables defined by the function $s = S(x)$ (which can be, in general, a vector function). This gives

$$\Phi(s) \sim -\frac{\sigma^2}{2} \log \rho_\sigma(s) = -\frac{\sigma^2}{2} \log \int dx \delta(S(x) - s) \rho_\sigma(x) \quad (8)$$

If the dimension of s is small, $\rho_\sigma(s)$ can be efficiently estimated, for example computing a histogram, see, e.g., Figs. 4 and 9. Its minima and saddle points can then be found straightforwardly, for example by visual inspection. However, this approach has an important drawback: the choice of the variables on which one performs the projection is arbitrary, and a wrong choice can bring to low-dimensional representations of Φ in which two or more attractors are erroneously merged. We will show later – see Fig. 9 – that the two-dimensional quasipotential of a realistic climate model estimated as a function of two *reasonable* variables has two clear local minima in a case in which the attractors are three.

To circumvent this problem one can perform the analysis with an approach borrowed from manifold learning, which allows estimating the quasipotential as a simultaneous function of a large number of variables (we will limit ourselves to $\mathcal{O}(100)$ in the case of this work, but the approach can be used seamlessly for many more) and studying its topography directly in this space. As we will show, this allows identifying the attractors of a dynamic system without preselecting a small number of putative important variables.

This procedure is rooted on a pretty general property of dynamical systems: even if the dynamics takes place in a D -dimensional space, where D can be very large, the trajectory is often contained in an embedding manifold whose dimension d is typically much smaller [92]; in the case of deterministic chaos this information is encoded by the Kaplan-Yorke dimension [93]. This, as we will see, makes the estimate of ρ_σ *restricted to the manifold* numerically and algorithmically possible. However, this manifold is typically twisted and curved, and it is very difficult (impossible, if the topology of the manifold is non-trivial) defining a global coordinate chart. In other words, a vector function $s = S(x)$ which is appropriate for estimating the quasipotential from Eq. (8) typically exists (and is d -dimensional) but it is very difficult finding it in practice. The approach we use allows estimating the quasipotential directly on the embedding manifold without defining explicitly the function $S(x)$.

Consider a trajectory \mathbf{x}_t , where t labels the different configurations. Consider the Euclidean distance $r_{t,t'} = \|\mathbf{x}_t - \mathbf{x}_{t'}\|$ between pairs of configurations. Even if this distance is defined in a D -dimensional space, if \mathbf{x}_t and $\mathbf{x}_{t'}$ are so close that one can neglect the curvature, $r_{t,t'}$

approximates a metric on the manifold. Building on this approximation, one first estimates d from the statistics of the ratio between the distance of the first neighbor $r_{t,(1)}$ of each data point t and the distance of its second neighbour $r_{t,(2)}$. One can prove that $\mu_t = \frac{r_{t,(2)}}{r_{t,(1)}}$ is Pareto distributed [62]: $\mu_t \sim \text{PD}(d)$, except for correction which depend on the curvature of the manifold and on the variation of the invariant measure on the scale of distance $r_{t,(2)}$. These errors vanish in the limit of infinite sample size [62]. This allows inferring the value of d from the empirical probability distribution of μ . See a closely related viewpoint based on the use of extreme value theory for study the recurrence properties of dynamical systems [94, 95].

The next step is estimating ρ_σ in each configuration x_t , or equivalently, the quasipotential $\Phi_t = -\frac{\sigma^2}{2} \log(\rho_\sigma(x_t))$. This is done using the approach in Ref. [63], a generalization of the k -Nearest Neighbor density estimator [96] in which the probability density is estimated implicitly on the embedding manifold and the optimal k becomes configuration-dependent. The optimal k is defined by finding by a statistical test the largest neighborhood of x_t in which the density can be considered constant with a given statistical confidence. We denote by \mathcal{N}_t this neighborhood and by \hat{k}_t the optimal value of k for configuration t . Φ_t is then obtained by maximizing a likelihood with respect to two variational parameters[63]:

$$\Phi_t = \operatorname{argmax}_\phi \max_a \left(-\phi \hat{k}_t + a \frac{\hat{k}_t(\hat{k}_t + 1)}{2} - \sum_{l=1}^{\hat{k}_t} e^{-\phi + al} v_{t,l} \right) \quad (9)$$

where, denoting by Ω_d the volume of a d -sphere of unitary radius and by $r_{t,(l)}$ the distance between x_t and its l -th nearest neighbour, $v_{t,l} = \Omega_d \left(r_{t,(l)}^d - r_{t,(l-1)}^d \right)$.

Importantly, this procedure provides, within the same statistical framework used for defining the likelihood in Eq. (9), an estimate of the error on Φ_t , which we denote by ε_t . As we will see, this allows assessing quantitatively the statistical reliability of the partition in attractors derived by the model.

The final step of the approach is inferring the topography of the quasipotential from the estimates Φ_t . This is done by using an unsupervised extension of Density Peak Clustering [64, 65].

Configuration t is assumed to be a local minimum of Φ if the following two properties hold: (I) $\Phi_t < \Phi_{t'} \forall x_{t'} \in \mathcal{N}_t$, namely if x_t is a minimum in \mathcal{N}_t (II) $t \notin \mathcal{N}_{t'} \forall t' : \Phi_{t'} < \Phi_t$, namely if x_t does not belong to the $\mathcal{N}_{t'}$ neighborhood of any configuration with lower Φ .

An integer label c is assigned to each of the n local minima found in this manner. The labels of the other configurations are found iteratively, by assigning to each point the same label of its nearest neighbor of smaller Φ [65].

The set of points with the same label c is denoted by \mathcal{A}_c and is assumed to correspond to an attractor. The

saddle points between the attractors are then found.

A configuration $x_t \in \mathcal{A}_c$ is assumed to belong to the border with a different attractor $\mathcal{A}_{c'}$ if it exists a configuration $x_{t'} \in \mathcal{N}_t \cap \mathcal{A}_{c'}$ such that $r_{t,t'} = \min_{x_{t''} \in \mathcal{A}_c} r_{t'',t'}$. The saddle point between \mathcal{A}_c and $\mathcal{A}_{c'}$ is the point of minimum Φ belonging to the border between the two attractors.

Finally, the statistical reliability of the attractors is assessed as follows. Denote by Φ_c the minimum value of Φ in the attractor c by ε_c its error, by $\Phi^{c,c'}$ the value of Φ of the saddle point between \mathcal{A}_c and $\mathcal{A}_{c'}$ and by $\varepsilon_{c,c'}$ its error. If $\Phi_{c,c'} - \Phi_{c'} < Z\sqrt{\varepsilon_c^2 + \varepsilon_{c,c'}^2}$, the attractor c' is merged with attractor c since the value of the quasipotential at its minimum and at the saddle point are indistinguishable at a statistical confidence fixed by the parameter Z [64]. The process is repeated until all the attractors satisfy this criterion, and are therefore statistically robust with a confidence Z .

This procedure is extremely helpful for detecting metastable states that might be masked in any low dimensional projection of the invariant measure. In the case the analysed data have been produced using a numerical model, it is possible to have conclusive results on the realism of a candidate attractor by running noiseless forward simulations from the best estimate of its position (and nearby points) as determined by the algorithm described above.

III. THE CLIMATE MODEL

We perform the numerical simulations that constitute the backbone of our investigation with PLASIM, an open-source intermediate complexity climate model developed by the group of Theoretical Meteorology at the University of Hamburg [51]. PLASIM has a total of roughly $\mathcal{O}(10^5)$ d.o.f., and retains some of the most important features of a climate system, but is considerably less sophisticated and cheaper to run than the present IPCC-class state-of-the-art Earth System Models that reach more than $\mathcal{O}(10^8)$ d.o.f., and require the use of supercomputing facilities [97]. PLASIM is extremely flexible and has been used for studying a rather extreme range of climatic conditions [46, 52–56], hence providing the perfect testing ground for novel theoretical investigations in climate science.

The dynamical core of PLASIM includes a set of primitive equations that are responsible for describing the mass and the budgets of momentum, energy, and water in the atmosphere and is based on its predecessor model, PUMA [19], which provides the dynamical core. The primitive equations are solved by the spectral transform method [98] in the horizontal, by finite differences in the vertical and for the time advancing scheme, a semi-implicit time stepping is used [99]. Further to that, unresolved physical processes, e.g. horizontal and vertical diffusion, long and short wave radiation, interaction with

clouds, moist processes and dry convection, precipitation, boundary layer fluxes of latent and sensible heat, and a land surface with biosphere are among the many to be effectively parameterized into the model. In that way, PLASIM simulates with a fair degree of accuracy all the necessary components of a realistic Earth-like climate system, with the notable exception of a dynamical component able to simulate the circulation of the ocean; see discussion in [45].

PLASIM is well-known to feature multistable dynamics, which has been observed and thoroughly studied in previous studies [8, 32, 53]. A simpler climate model that conceptually sits between PUMA and PLASIM has been used to perform accurate analysis of the global stability properties of the climate systems [33, 37, 57] and has inspired the present study. Compared to such studies, the model used here is much closer to an actual state-of-the-art climate model as it includes – yet in a somewhat simplified way – a much more sophisticated representation of processes like radiation, hydrological cycle, clouds, water phase changes, and surface processes. As it will become apparent below, the presence in PLASIM of a reasonably realistic representation of the hydrological cycle introduces here a new layer of complexity in the present study, by emphasizing the nonequilibrium properties of the system we are investigating.

A. Experimental configuration

Our experimental configuration uses a present day geography and further consists of an oceanic mixed layer of 50 m depth via a one-layer slab ocean model, which includes a thermodynamic sea-ice module [100]. Furthermore, we neglect contributions from continental ice-sheets, vegetation and interactive carbon cycle. The resolution of the model is T21 in the horizontal direction, corresponding to a $5.6^\circ \times 5.6^\circ$ grid cell, with 10 levels in the vertical, while the time-step is 45 min. Finally, we fix the CO_2 concentration to 360 ppm, while daily and seasonal cycles have been purposefully neglected to further remove any explicit time dependency of the evolution equations in the reference state.

We are interested in noise induced global climatic transitions, driven primarily by the imposed random fluctuations of the solar constant, in a similar spirit as in [37, 57].

The noise is here introduced as yearly fluctuations of the solar constant, following a Gaussian distribution with a mean close to the present-day value, equal to $S^* = 1365 \text{ W/m}^2$. We perform a series of long single trajectory simulations, with each having a different standard deviation δS , defined as a fraction of the mean $\delta S = \sigma S^*$, where $0 < \sigma < 1$. Spanning from $5 \cdot 10^3$ to $6 \cdot 10^4$ years duration, this recipe allows to sufficiently explore the phase space of the system for different noise intensities. Note that when weaker noise is considered, one needs to evolve the system for a larger amount of time, as the transitions between the basins of attraction become more rare.

We configure two experimental setups that differ in terms of how the oceanic heat transport is prescribed. In setup A the horizontal ocean diffusion is active and its parametrization requires choosing a specific value for the horizontal diffusivity constant. This setup allows for a simple yet effective representation of the impact of the large-scale ocean transport on the climate as a whole, and has been used in a recent study where response theory was used to perform climate projections [46]. In setup B, the horizontal ocean diffusivity is set to 0, which implies that the associated feedback to the large scale heat transport performed by the ocean is neglected. A similar configuration as in setup B has been previously employed to study the thermodynamic properties of the climate system in response to controlled changes of the solar constant [32] or of the CO₂ concentration [52, 55].

IV. RESULTS

A. Setup A – Atmospheric and Oceanic Large Scale Energy Transport

1. The Two Competing Climate States

The setup A of the model is such that the slab ocean is able to transport energy poleward thanks to the presence of a horizontal diffusion. The representation of the large scale oceanic energy transport is, euphemistically, oversimplified compared to what really occurs in Earth, as our model cannot represent the process of deep water formation and the large scale circulation of the ocean [101–103]. Nonetheless, the presence of horizontal heat diffusion performed by the ocean has the great merit of introducing an additional mechanism – on top of atmospheric transport fuelled by baroclinic instability – that contributes to reducing the large scale temperature difference between low and high latitudes [1, 104–106]. We find, as expected, two competing asymptotic states corresponding to the W and SB climates, in agreement with a plethora of previous investigations, as discussed in the introduction.

In Fig. 2 we present the zonally averaged annual mean of a 40-year long time-series of several observables, computed when steady state conditions are realized. We compare here zonally averaged fields of the W climate (red lines) and of the SB (blue lines); additional information on globally averaged quantities are presented in Table I.

Fig. 2(a) shows the climatology of the zonal mean surface temperature. In agreement with previous studies performed on PLASIM [8, 32, 53], the SB state features global glaciation and extremely low temperatures at all latitudes, while the W state is similar to the present-day climate; see also the map of sea-ice cover in Fig. 3, where the limit of sea-ice approximately coincides with the isoline of 0° C in the surface temperature shown in Fig. 2(a).

Figure 2(b) shows the annual mean budget of the pre-

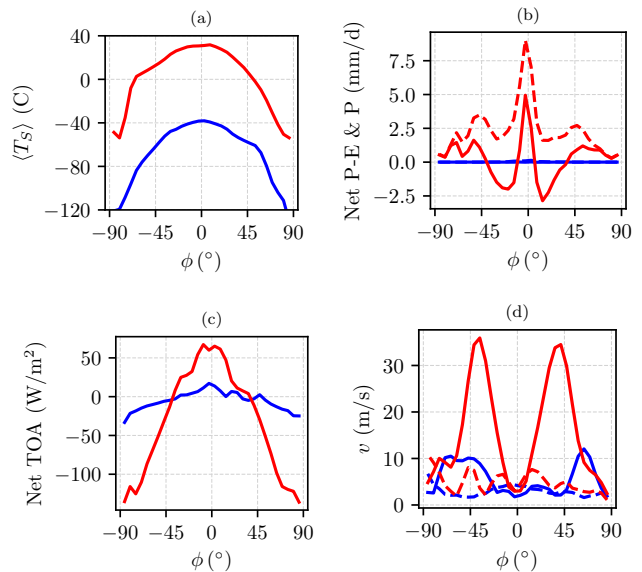


FIG. 2. Climatological longitudinally averaged annual mean of (a) surface temperature, (b) Precipitation minus Evaporation (P-E, solid lines) and Precipitation (P, dashed lines), (c) top of the atmosphere net radiation, (d) magnitude of zonal wind speed at 300 hPa (solid lines) at 1000 hPa (near surface, dashed lines) versus the latitude ϕ . Blue lines: SB state. Red lines: W state.

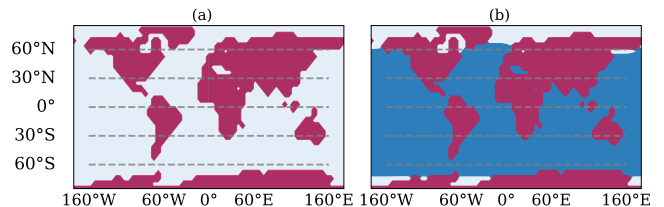


FIG. 3. Sea-ice coverage comparison between (a) snowball and (b) warm climates. We depict the land-map used by our model.

cipitation minus evaporation rate (P-E) as well as the annual zonally averaged precipitation. The SB climate is almost entirely dry, as a result of the fact that the very low temperature of the atmosphere permits the presence of nothing but an extremely small amount of water vapour, because of the constraint posed by the Clausius-Clapeyron relation [1]. The W climate has the familiar maximum of precipitation in the equatorial belt and secondary peaks in the mid-latitudes, resulting from convective precipitation and synoptic disturbances, respectively. The P-E field describes the scenario of net water vapour transport from the tropics into the equatorial belt and into the mid-latitudes [1].

Figure 2(c) shows the zonally averaged net TOA energy budget, which is the sum of the incoming shortwave radiation and the outgoing longwave radiation and scattered shortwave radiation. Note that the fluxes are positive when entering the planet and negative when

leaving the planet. At steady state, the zonal TOA energy imbalance is compensated by the divergence of the meridional atmospheric enthalpy transport [1, 104, 105]. We then conclude that such a transport is much stronger for the W state, where large contributions come from baroclinic eddies and from the large scale transport of water vapour. Baroclinic eddies are located in the region of the jet, where zonal winds in the upper troposphere at 300 hPa (near the tropopause, where the peak intensity is found) – Fig. 2(d) – and their existence is made possible by the conversion of available potential into kinetic energy via baroclinic instability, which is associated to the presence of a substantial meridional temperature difference between low and high latitudes in the atmosphere. The vigorous circulation of the W state corresponds to a powerful Lorenz energy cycle [107] ($\approx 3.4\text{W m}^{-2}$). Instead, the meridional enthalpy transport and the zonal circulation of the SB state are extremely weak, corresponding to the presence of very modest meridional temperature gradients [8, 32, 53]. The SB state features a very weak Lorenz energy cycle ($\approx 1.0\text{W m}^{-2}$), as the presence of a weak meridional temperature gradient leads to the presence of a scarce reservoir of available potential energy and shuts down almost entirely the mechanism of baroclinic instability. The presence of a vast difference in the intensity of the Lorenz energy cycle in the two climates corresponds to the presence of much weaker surface winds in the SB than in W climate; see Fig. 2(d).

TABLE I. Main climatic features of the stable climates for the two experimental configurations, where A refers to setup A, and B to setup B; W for warm state, C for cold state, and SB for snowball state; LEC stands for Lorenz energy cycle.

	$\langle T_S \rangle$ ($^{\circ}\text{C}$)	ΔT_{EP} ($^{\circ}\text{C}$)	sea ice (%)	LEC (W/m^2)
A W	15.0(2)	26.4(3)	5.5(1)	3.39
A SB	-55.2(3)	25.7(5)	100	1.00
B W	4.4(3)	40.0(5)	27.7(1)	4.79
B C	-28(2)	53(1)	70(2)	3.79
B SB	-52.5(5)	25.9(5)	100	1.19

2. Noise-induced Transitions

As mentioned earlier, PLASIM features a total of roughly $\mathcal{O}(10^5)$ d.o.f.. In what follows, we will apply a very severe coarse-graining to the phase space of the model. Indeed, we consider as relevant variables the globally and monthly averaged surface temperature $\langle T_S \rangle$ and monthly averaged Equator minus Poles surface temperature difference $\Delta T_{EP} = \langle T_{Eq} \rangle - \langle T_{Po} \rangle$, where we denote the spatial average of the field X by $\langle X \rangle$, and the temporal average by $\langle X \rangle$. Note that $T_{Eq} \equiv [T_S]_{0^{\circ}}^{30^{\circ}}$, implying that the spatial average is taken in the latitudinal belt $[0,30\text{N}]$ together with the corresponding symmetric counterpart $[30\text{S},0]$, and accordingly for the Poles sur-

face temperature it holds $T_{Po} \equiv [T_S]_{30^{\circ}}^{90^{\circ}}$. Reducing the phase space like this provides a minimal, yet still physically relevant description of the system, as discussed in [33, 37, 57, 74]. Indeed, variations in the globally averaged surface temperature reflect, to a first approximation, changes in the energy budget of the planet (warming vs cooling), while ΔT_{EP} controls the large scale energy transport performed by the geophysical fluids [1, 105].

The nonequilibrium steady state of the system in absence of any form of stochastic forcing corresponds to either of the attractors described above. The asymptotic state is determined by the initial condition, and escape from the basin of attraction is, by definition, impossible. As stated earlier, though, transitions between the attractors can be induced by noise. In Fig. 4(a) we present the projection of the invariant measure on the reduced phase space spanned by $\langle T_S \rangle$ and ΔT_{EP} (normalized to one), while in Fig. 4(b), following [61, 84], we approximately estimate the corresponding quasipotential using Eqs. (4) and (8):

$$\Phi(\langle T_S \rangle, \Delta T_{EP}) \sim -\frac{\sigma^2}{2} \log \rho_{\sigma}(\langle T_S \rangle, \Delta T_{EP}). \quad (10)$$

Notice that we subtract the absolute minimum from $\Phi(\langle T_S \rangle, \Delta T_{EP})$ to shift to zero the level of the deepest quasi-potential well. In both cases $\sigma = 18\%$, which is the weakest noise considered for setup A that allows us to observe a sufficient number ($\mathcal{O}(40)$) of $SB \leftrightarrow W$ transitions within a – for us – reasonably long ($\mathcal{O}(3 \cdot 10^4 y)$) simulation. The estimate of the quasi-potential does not change significantly when considering the output of simulations performed with higher ($\sigma = 20\%$) intensity of the noise, thus suggesting that the weak-noise approximation is valid. We find that the basin of the W attractor is deeper (lower values of the quasi-potential) compared to the basin of the SB attractor. By using Eq.(7) and performing an exponential fit of the statistics of average residence times in the two attractors for different values of the noise intensity – see Fig. 4(c), we obtain the following information on the two local potentials: $\Delta\Phi_{W \rightarrow SB} \approx 700(40)$ and $\Delta\Phi_{SB \rightarrow W} \approx 240(50)$.

Another relevant piece of information can be obtained by looking at the paths of the $SB \rightarrow W$ and $W \rightarrow SB$ transitions. In the weak-noise limit, the stochastic average of the trajectories that manage to escape from either attractor gives the instantonic path for the portion of trajectory connecting the attractor to an M state, and the relaxation path for the remaining part of the trajectory, which connects the M state to the other attractor. The red (blue) line in Fig. 4(b) indicate the stochastic averages of the $SB \rightarrow W$ ($W \rightarrow SB$) transition trajectories. The procedure for computing the average paths is described in detail in the SM.

As discussed above, escape trajectories and relaxation trajectories are expected to follow different paths in general nonequilibrium systems. We are indeed able to find such an essential feature of nonequilibrium systems, as clear from Fig. 4(b). In simpler setups with a unique

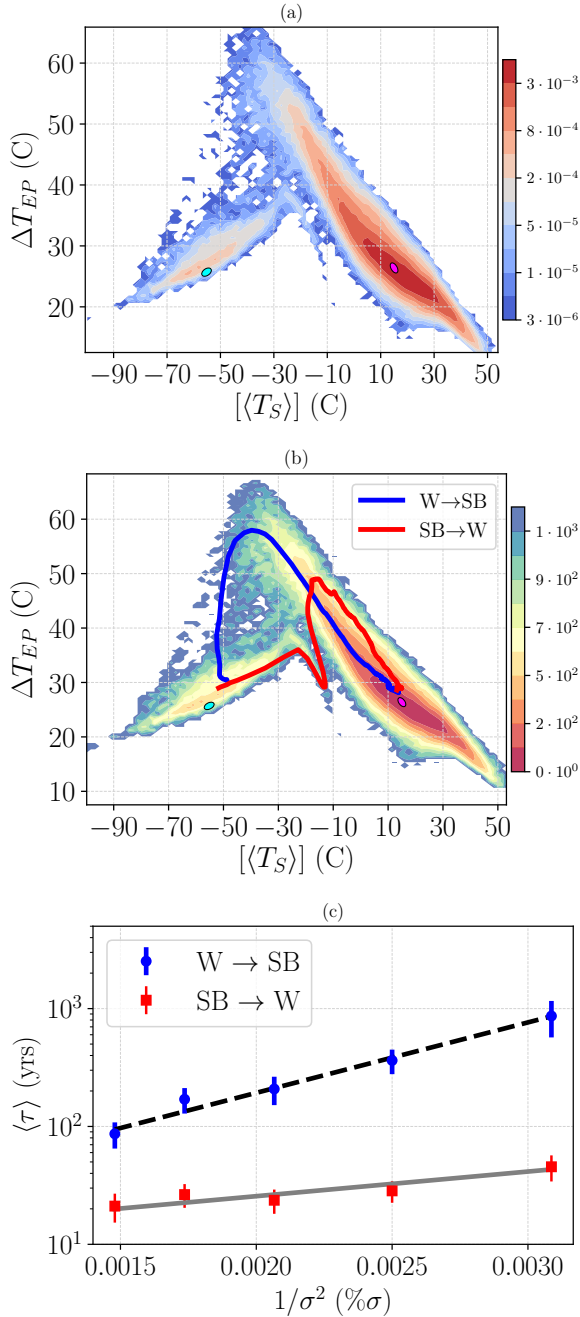


FIG. 4. (a) Projection of the invariant measure on the reduced phase space spanned by the 30-day averaged global temperature versus 30-day averaged Equator to pole temperature difference for setup A and $\sigma = 18\%$. (b) The corresponding quasipotential, shifted so that the global minimum is set to 0. The blue and red lines correspond to stochastically averaged transition paths for the $W \rightarrow SB$ and $SB \rightarrow W$ transitions. These trajectories follow different escape and relaxation paths, within each basin of attraction. The colored ellipses indicate the location of the deterministic attractors corresponding to SB state (cyan), and W state (magenta). (c) Average escape time versus the inverse squared $\% \sigma$ in setup A, where dashed black and straight gray lines correspond to fitting Eq. (7).

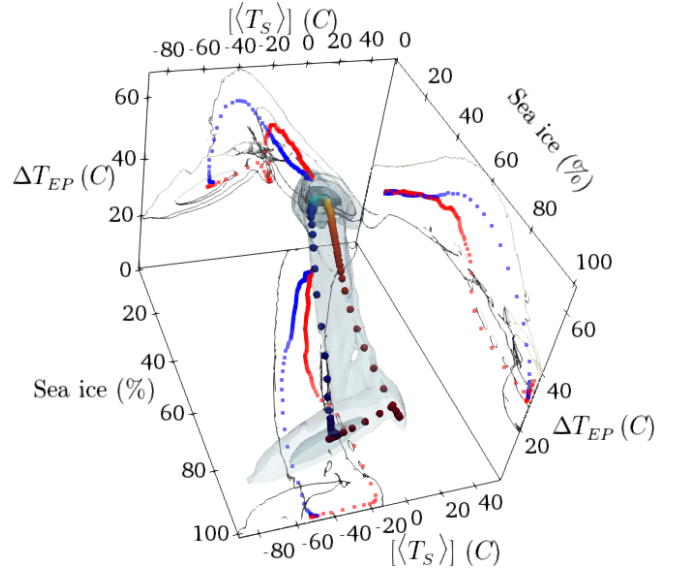


FIG. 5. Transitions paths $SB \rightarrow W$ (red) and $W \rightarrow SB$ (blue) in the 3D/2D space spanned by the 30-day averaged global temperature, the 30-day averaged Equator to pole temperature difference, and the arctic sea ice percentage for setup A and $\sigma = 18\%$. The shading indicates the density of the projected invariant measure, while a 2D projection of the transition paths in each plane is added for further comparison, see Fig. 4b).

saddle, the crossing point between the red and the blue line must correspond to the position of the M state, see discussion in [37, 57].

Instead, this is not the case here, as the crossing between the two transition paths as observed in Fig. 4 is an artifact of looking at that specific two-dimensional projection, as can be noticed from Fig. 5. The $SB \rightarrow W$ and the $W \rightarrow SB$ transitions go through two different channels corresponding to two different M states. This marks a major difference with respect to the analysis performed in [37, 57]. We have clear indication that the model used in this study has a fundamentally more nonequilibrium behaviour, because large scale currents are present in the phase space.

It is reasonable to ascribe such a difference to the fact that here we are able to include a large class of processes associated with the transport of water and with its phase changes between solid, liquid, and gaseous forms. Indeed, the hydrological cycle is greatly responsible for the irreversibility of atmosphere [2, 108, 109] and, at more quantitative level, overwhelmingly contribute to the total entropy production of the geophysical fluids compared to the dissipation of kinetic energy and the turbulent exchange of sensible heat [52, 53, 110, 111]. We argue that the lack of a comprehensive treatment of water in the model used in [37, 57] leads to an underestimation of the actual entropy production of the system, which makes it closer to equilibrium than the model considered here. According to a statistical mechanics angle, one sees this

as associated with the absence (or significant reduction) of probability currents, which are suppressed by the presence of a single saddle separating the competing basins of attraction.

Phenomenologically, the presence of clear distinction between the $SB \rightarrow W$ and the $W \rightarrow SB$ transition paths clearly indicates that the global thawing and the global freezing of the planet are fundamentally different processes. This can be better appreciated by watching the movies portraying the transitions between the two competing states included in the SM.

The thawing proceeds as follows. First, because of persistent positive anomalies of the solar irradiance, the global temperature of the planet grows without much changes in ΔT_{EP} , because the atmospheric circulation is extremely weak and the oceanic transport absent. Then, the equatorial belt starts to melt and, because of the large decrease of the albedo in the equatorial band and subsequent intense warming, ΔT_{EP} increases substantially – see the almost vertical portion of the red line in Fig. 4b). This leads to a strong enhancement of the meridional heat transport performed by the atmosphere and by the ocean, which causes to thawing of the sea-ice at higher latitudes until the sea-ice line reaches very high latitudes compatible with the W climate.

The global freezing of the planet, instead, proceed in the following way. The cause of the freezing is, obviously, the presence of a (rare) persistent negative anomaly of the solar irradiance. The reduction of incoming solar radiation has an amplified effect at high latitudes, because of the ice-albedo effect, leading to an increase of ΔT_{EP} . The increase in ΔT_{EP} causes a strengthening in the meridional heat transport, as discussed above, which acts as a stabilizing feedback – see the diagonal portion of the blue line in Fig. 4b). Nonetheless, if the anomaly in the solar irradiance is sufficiently strong and persistent, the sea-ice line moves equatorward, until the equatorial belt freezes and undergoes further extreme cooling because the albedo becomes very high, leading eventually to a very low value of ΔT_{EP} in the final SB state.

3. Relaxation Modes

As detailed in the SM, by suitably constructing a finite-state Markov chain model, it is possible to extract further useful information about the slow dynamics of the system. We study the statistics of the transitions of the state of the system for the case $\sigma = 18\%$ on a time scale of 1 month in the $([\langle T_S \rangle], \Delta T_{EP})$ space. The dominant eigenvector of the Markov chain is the projection of the invariant measure given in Fig. 4a). The subdominant eigenvectors describe the relaxation of a generic initial measure to the invariant one. Their integral vanishes, as discussed in Sec. III of the Supplementary Material, and we normalise them in such a way that the integral of their absolute value is 1. We remark that, despite the very severe projection, the Markov chain model features

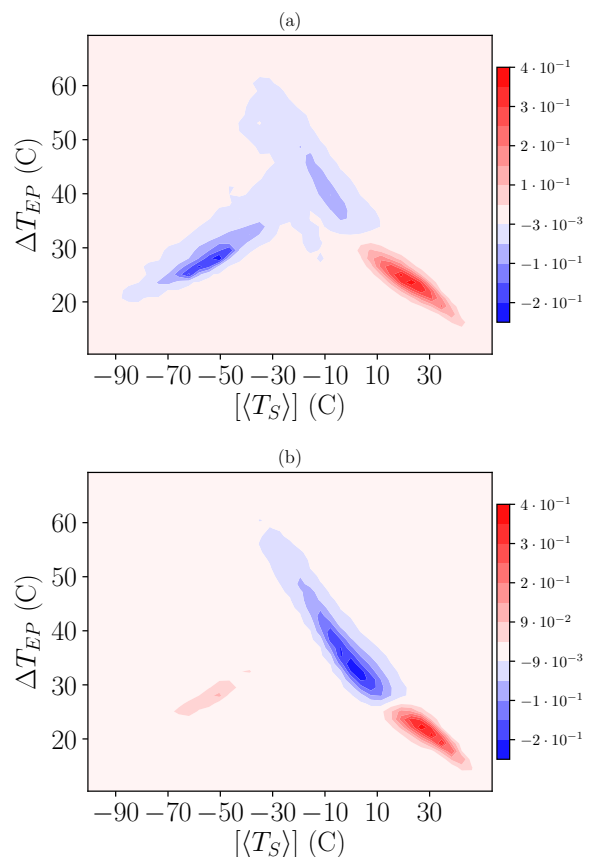


FIG. 6. First two subdominant eigenvectors of the finite state projected Markov operator for setup B and $\sigma = 18\%$. a) First subdominant mode ($\tau \approx 30y$) describing the transitions between the two competing metastable states; see also a clear signature of persistent cold departures of the system – within the warm attractor – from typical warm conditions leading to the transitions. This special region within the warm attractor is likely to be a left-over of the third attractor realized for setup A. b) Second subdominant mode ($\tau \approx 11y$) describing the low-frequency variability within the warm attractor. Note the lack of time-scale separation between these two modes.

positive metric entropy, which measures the rate of creation of information, and positive entropy production, which unequivocally indicates nonequilibrium conditions and is associated to the presence of currents [112].

The two leading subdominant eigenvectors of the finite-state Markov chain approximation of the projection of the transfer operator in the $([\langle T_S \rangle], \Delta T_{EP})$ plane for the case $\sigma = 18\%$ are presented in Fig. 6a)-b). Panel a) describes – in statistical terms – the coarse grained, slow process of transition between the two metastable states. One of two peaks is negative and the other one is positive, as the mode describes a zero-sum probability transfer. Additionally, this eigenvector has a very clear signature of persistent excursions of the system in the far cold region of the warm attractor. This might be interpreted as a signature of the preferential regions where transitions between the SB and W states take

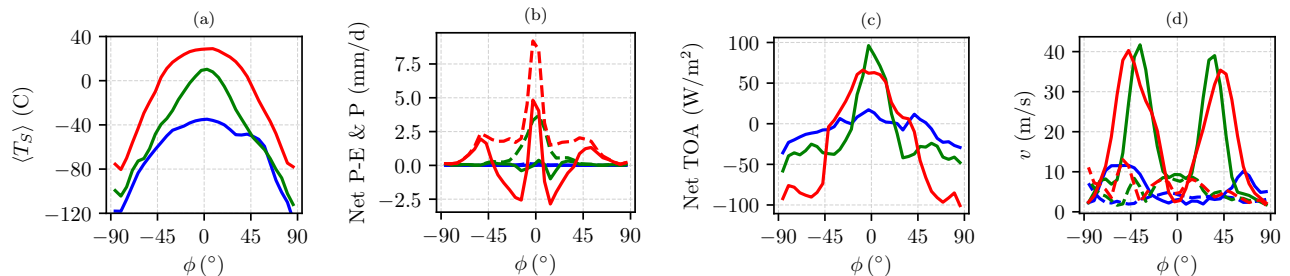


FIG. 7. Climatological longitudinally averaged annual mean of (a) surface temperature, (b) Precipitation minus Evaporation (P-E, solid lines) and Precipitation (P, dashed lines), (c) top of the atmosphere net radiation, (d) magnitude of zonal wind speed at 300 hPa (solid line) and at 1000 hPa (near surface, dashed lines) versus the latitude ϕ . Blue lines: SB state. Red lines: W state. Green lines: C state.

place, compare with Fig. 4b).

Instead, panel b) by and large describes the slowest intrawell variability, which takes place in the *W* attractor: the two closely spaced peaks of opposite sign are on the opposite sides of the peak of the warm attractor, with the zero isoline cutting across the peak of the warm attractor, compare Fig. 4a). This slow time scale is associated with the process of ice formation and melting. A smaller peak is present in correspondence to the *SB* attractor, indicating that this eigenvector captures some $W \rightarrow SB$ escape process, compare with Fig. 4b).

B. Setup B – Atmospheric-only Large Scale Energy Transport

1. The Three Competing Climate States

Excluding the large-scale heat oceanic transport amounts to removing a very powerful negative feedback, i.e. a mechanism of stabilization for the climate that efficiently redistributes energy throughout the system. This changes qualitatively the global stability properties of the system compared with the case of setup A. Indeed, in setup B we find three competing climate states, whose basic features are reported in Table I, and we refer to Fig. 2 in the Supplementary Material for further evidence. One of the climates is the fully-glaciated SB state, which features very low ΔT_{EP} and extremely low global temperature, close to -50 °C. The second climate resembles the *W* state found in setup A, featuring an above 0 °C global temperature, with $\Delta T_{EP} \approx 40$ °C and roughly 27% sea ice coverage.

Between the two, lies the – unexpected and unprecedented for PLASIM – C state, which is not fully ice covered, and even though it has $\langle T_S \rangle \approx -30$ °C, the fact that $\Delta T_{EP} \approx 50$ °C indicates the possibility of a warm latitudinal band being present at subtropical latitudes, as discussed below. The presence of an ice-free latitudinal band has huge implications in terms of habitability [34, 113].

In Fig. 7 we compare the climatology of the three cli-

mates (*W* in red, *C* in green and *SB* in blue). The *SB* state is very similar to the one obtained with setup A, as the ocean plays a negligible role in a fully glaciated planet, and will not be further discussed here. The *W* state is similar to what found in setup A, albeit considerably colder, and, correspondingly, with a weaker hydrological cycle. We can interpret this as resulting from the ice-albedo feedback. Indeed, the presence of a weaker heat transport towards high latitudes due to removing the oceanic channel of meridional transport leads to a larger sea-ice surface – compare the top right panel in Fig. 3 with the corresponding one in Fig. 8 – which contributes to lowering the planetary albedo, thus enhancing the input in the energy channel at TOA. By Boltzmann radiation feedback, the steady state must then be characterized by a lower average temperature. Finally, the presence of larger temperature differences between high and low latitudes lead to a stronger atmospheric variability, as baroclinic conversion is more efficient and can draw from a larger reservoir of available potential energy. This is associated with a stronger Lorenz energy cycle compared to setup A, see Table I. The climatic effects of modulating the meridional oceanic heat transport in the *W* state have been discussed in detail in [106], yet in a slightly different experimental setting.

Fig. 7(a) shows the climatology of the zonal mean surface temperature. We remark that in the *C* state the subtropical band $[-20^\circ N, 20^\circ N]$ features above-freezing temperature, while lower temperatures, and correspondingly, prevailing sea-ice is present at higher latitudes, as shown in Fig. 8.

The *C* states shares features of the previously discussed Slushball state [114] and, especially, of the Jormungand state [69], where the presence of ice-free equatorial band is associated with the dynamics of continental ice sheets and of the interplay of sea-ice cover, surface albedo, and atmospheric circulation, respectively.

Figure 7(b) shows the annual mean budget of the precipitation minus evaporation rate (P-E) as well as the annual zonally averaged precipitation. The *C* state features an intense precipitation in the equatorial belt, driven by the strong convection occurring there, but the P-E field

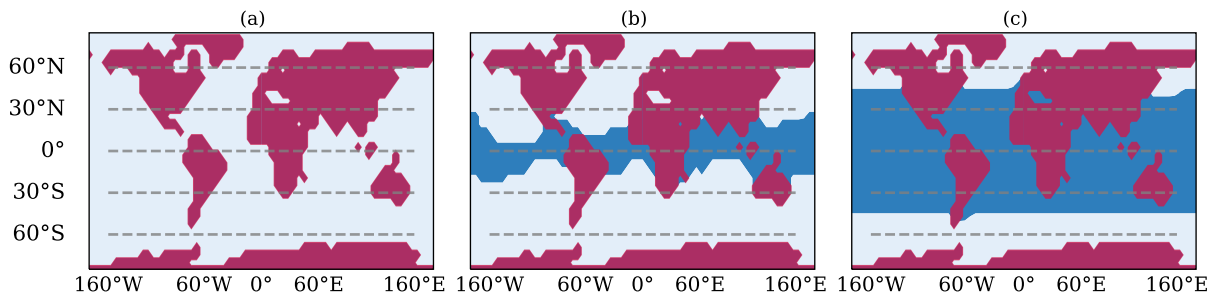


FIG. 8. Sea-ice coverage comparison between (a) snowball, (b) cold and (c) warm climates. Note that the W state of setup B has more sea-ice than the W state of setup A.

indicates that the water vapour is recycled and no large scale transport takes place, as opposed to the W state.

Figure 7(c) shows the zonally averaged net TOA energy budget. One can infer that the meridional atmospheric enthalpy transport has comparable intensity in the W and C climates, yet the peaks of the transport – indicated by vanishing values of the TOA budget [1, 104, 105]– are confined to lower latitudes in the latter case. This indicates a vigorous heating realized at $\approx \pm 30^\circ N$.

Correspondingly, the jet stream for the C state is located at lower latitudes compared to the W climate (panel d), while it is more intense, as the local meridional temperature gradient throughout the atmosphere is larger. This corresponds to a large temperature difference between low and high latitudes at surface, see Table I.

The C state features a strong Lorenz energy cycle ($\approx 4.0 \text{ Wm}^{-2}$), thanks to the presence of such large meridional temperature gradients which correspond to a large reservoir of available potential energy that can be converted to kinetic energy by baroclinic instability. The intensity of the Lorenz energy cycle of the C state is especially remarkable given that the atmospheric circulation is relatively weak poleward of 50° latitude.

2. Noise-induced Transitions

The presence of three instead of two deterministic attractors makes setup B considerably more complex than setup A, because now we have to take into account the existence of extra M states connecting SB with C and W with C, on top of the one connecting SB with W seen already in setup A. Figures 9(a)-(b) mirror the corresponding panels of Fig. 4. Panel a) shows the projection of the invariant measure in the reduced phase space given by $([\langle T_S \rangle], \Delta T_{EP})$ obtained for $\sigma = 12\%$, while in Fig. 9(b) we show the estimate the quasipotential. We remark that in setup B a lower noise intensity is needed to excite transitions with frequency comparable to what obtained in setup A, for the basic reason that we are missing the global stabilizing feedback given by the ocean heat

transport. This corresponds to having weaker diffusion in the Fokker-Planck operator describing the evolution of probabilities. The location of the deterministic attractors is shown with ellipses of different color, where magenta, green and cyan correspond to W, C and SB climate states, respectively.

The location of the C state is not directly visible in the projected invariant measure or in the quasi-potential, in the form of a local maximum and minimum, respectively. The operation of performing a projection to such a low-dimensional space is mainly responsible for such a loss of information. This issue is addressed specifically in Sec. IV C. Additionally, as we shall see below, the third attractor corresponds to a much shallower local minimum of the quasi-potential compared to the W or SB states. As a result, the C local minimum is washed out when considering a noise intensity of $\sigma = 12\%$, and it is hard to keep track of orbits persisting significantly near C, see Eqs. (4)-(7). This implies the presence of an additional scale relevant for understanding the multistability of the system, along the lines of what depicted in Fig. 1.

As mentioned above, the presence of ocean diffusion triggers the ice-albedo feedback in a direction that favours warming. Accordingly, in setup B, the minimum of the quasipotential corresponding to the SB state is deeper than the one corresponding to the W state. This can be further quantified in Fig. 10(a), where the $SB \leftrightarrow W$ mean escapes times $\bar{\tau}_\sigma$ are presented as a function of the inverse squared noise amplitude. After performing the exponential fit of Eq.(7), we obtain the following estimates for the depth of the local quasi-potentials: $\Delta\Phi_{W \rightarrow SB} \approx 290(10)$ and $\Delta\Phi_{SB \rightarrow W} \approx 500(10)$. We remark a major difference with respect to the corresponding figure for setup A: the pre-exponential factors of the expectation value of escape times is in this case vastly different. Note that, neglecting the C state, the population of the SB and W state is inversely proportional to the corresponding escape times. As a result, despite being associated to a shallower local minimum of the quasi-potential, the fraction of population in the W state is larger when considering relatively strong noise intensity, whereas eventually, the SB state dominates in the weak-noise limit. Despite the profound dynamical differ-

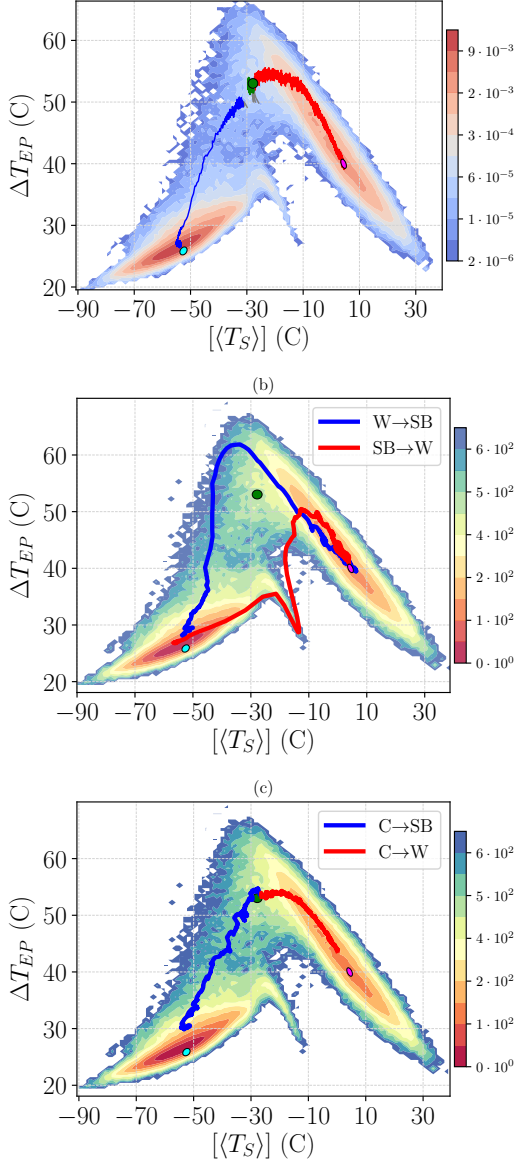


FIG. 9. (a) Projection of the invariant measure of the system in reduced phase space composed of the 30-day averaged global temperature versus 30-day averaged Equator to pole temperature difference for setup A and $\sigma = 12\%$. (b) The corresponding quasipotential, shifted so that the global minimum is set to 0. The blue and red lines correspond to stochastically averaged transition paths for the $W \rightarrow SB$ and $SB \rightarrow W$ transitions. The trajectories are completely different, depending on the direction of the transition. The ellipses indicate the location of the deterministic attractors corresponding to the SB state (cyan), the C state (green) and the W state (magenta). (c) Same as in (b), but now showing the stochastically averaged escapes from the C state with $\sigma = 6\%$.

ences between setup A and B, the estimates of the instantonic and relaxation paths between the SB state and the W state are qualitatively similar; compare Figs.4(b) and 9(b). Furthermore, the interpretation of the different

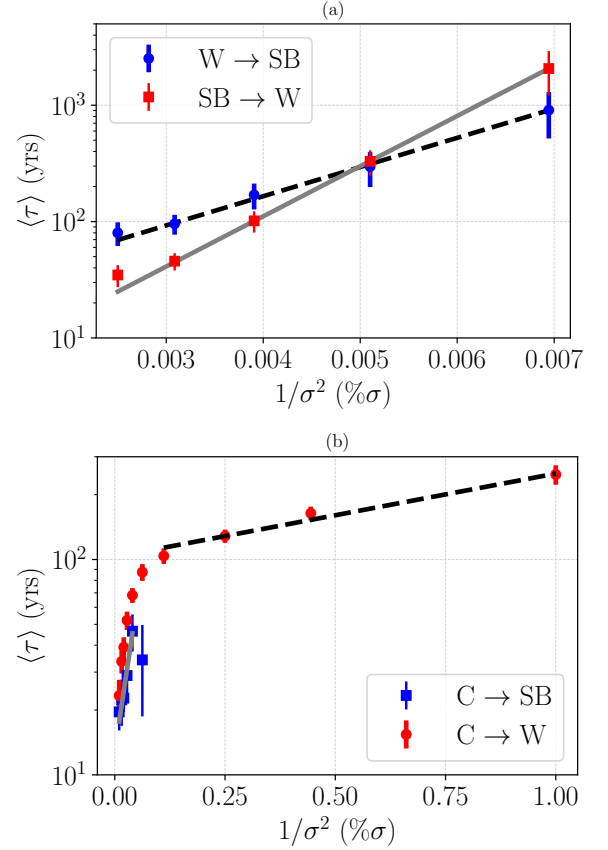


FIG. 10. Average escape time versus the inverse squared $\% \sigma$ in setup A. (a) Comparison of $W \rightarrow SB$ (filled blue circles) and $SB \rightarrow W$ (filled red squares) and corresponding exponential fit, black dashed and gray straight lines. (b) Comparison of $C \rightarrow W$ (filled red circles) and $C \rightarrow SB$ (filled blue squares) and corresponding exponential fit, black dashed and gray straight lines. The fitting expression is given by Eq. (7).

physical mechanisms controlling the $SB \rightarrow W$ and $W \rightarrow SB$ transitions paths for setup B is fundamentally the same as described earlier for setup A. We remark that the time scale of the trajectories used to estimate the $SB \rightarrow W$ and $W \rightarrow SB$ transition paths are longer by a factor of about 2 with respect to setup A.

The more complex geometry of the phase space of setup B is furthermore made apparent by the fact that (as can be seen in the movies included in the SM), while in some cases the transitions between the W and SB states are direct and the C state is bypassed, in other cases the paths deviate considerably as the orbit is temporarily trapped near the C state. We remark that this trapping is always extremely short-lived compared to the other relevant time scales associated with the transition between the two other metastable states.

The next step is to provide a characterization of the quasi-potential near the C state, and, specifically, to estimate the $C \rightarrow SB$ and $C \rightarrow W$ barriers for the local quasi-potential. In order to get around the curse of the mul-

tiscable nature of the multistability, which entails that no selection of noise is suitable for getting a complete picture of the system, because it is either too large or too weak for discovering some features of the quasi-potential, we proceed as follows. Following [57], we investigate the escape process from the C state by considering a large number of trajectories initialized in the deterministic C attractor and apply a weaker random forcing with $\sigma = (1\% - 10\%)$. Further comments on the escape from the C state can be found in the SM. We then collect the statistics of escape times and keep a separate track for trajectories ending up in the W versus in the SB state through the corresponding M states. Using Eq. (7), we are able to estimate the two quasi-potential barriers $\Delta\Phi_{C \rightarrow SB}$ and $\Delta\Phi_{C \rightarrow W}$. We see in Fig. 10(b) that $\Delta\Phi_{C \rightarrow SB} \approx 16(2)$ (blue filled squares) is about one order of magnitude smaller than the $W \leftrightarrow SB$ barriers. Interestingly, the energy barrier $\Delta\Phi_{C \rightarrow W} \approx 0.45(4)$ (red filled circles) turns out to be much smaller than $\Delta\Phi_{C \rightarrow SB}$, which explains why below a certain noise level, i.e. $\sigma \approx 4\%$ we practically get no transitions towards the SB attractor, with all escape trajectories ending in the W attractor. Also, for the $C \rightarrow W$ transitions, we clearly observe from Fig. 10(b) that for σ larger than $\sigma \approx 5\%$ there is a different scaling that can be attributed to the prefactor in Eq. (7), which is a signature of the fact that the weak noise limit has not been achieved for these values of σ .

3. Relaxation Modes

Finally, we study the two subdominant eigenvectors of the finite-state Markov chain approximation of the projection of the transfer operator in the $([\langle T_S \rangle], \Delta T_{EP})$ plane for the case $\sigma = 12\%$, see Fig. 11a)-b). As for setup A, the Markov chain model features positive metric entropy and positive entropy production. We get a broad agreement with what shown for setup A also in terms of interpretation of the meaning of the eigenvectors, but we have in this case a much clearer separation of scale between the two corresponding eigenvalue. The first subdominant eigenvector has a much longer life-time of approximately 290 years (panel a), which matches the life time of the SB state. Because of such a long time scale, and of the fact that the actual time it takes the system to cross over the M state is small compared to the permanence in either the SB or M state, we lose any feature of the transition path, as opposed to what found for setup A. The eigenvector shown in panel b) has a life-time of about 10 years and portrays the low-frequency variability in the W state, which can lead to occasional transitions towards the SB state, compare the $W \rightarrow SB$ transition path in Fig. 9b). We find no signature of the presence of the C state, whose life time is much smaller than 10 years for this level of noise. These eigenvectors further clarify that for this level of noise the C state is almost entirely washed out.

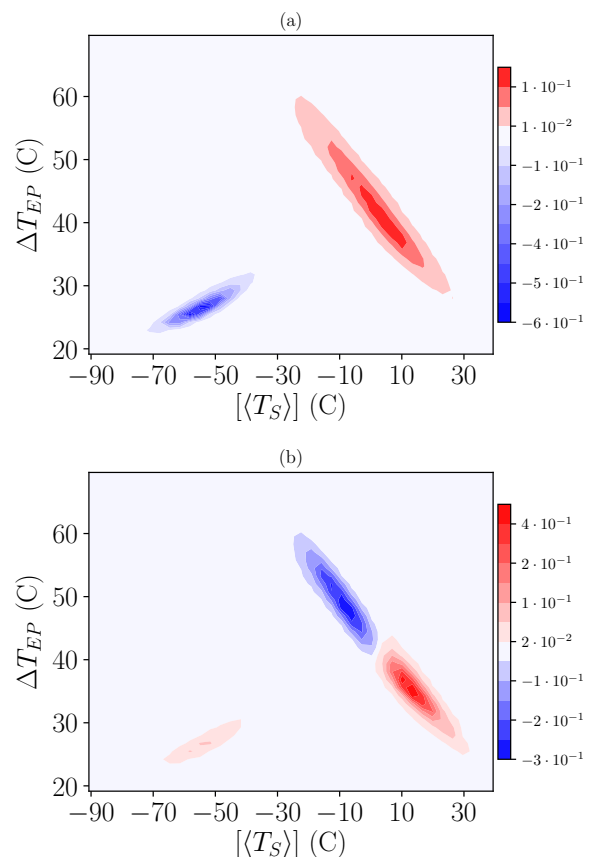


FIG. 11. First two subdominant eigenvectors of the finite state projected Markov operator for setup A and $\sigma = 12\%$. a) First subdominant mode ($\tau \approx 290y$) describing the transitions between the two main competing metastable states. b) Second subdominant mode ($\tau \approx 10y$) describing the low-frequency variability within the warm attractor. Note the lack of any signature of the cold attractor, whose lifetime is much shorter than 10 y.

C. Automatic determination of the metastable states

The previously discussed results have been obtained using the – methodologically standard – top-down approach based on the careful use of targeted numerical simulations, differing for the chosen intensity of stochastic forcings or altogether neglecting it.

The basic issue we want to solve is that, while in Fig. 9 the SB and W state clearly appear as corresponding to local maxima of the projected invariant measure, this is not the case for the C state, in this as well as in many other 2D projections we have tested. Indeed, it has been impossible with the tools developed so far to find any direct evidence of the C state in the stochastic integrations. As described in Sect. IV B 1, the discovery of the C state has been serendipitous and based on the exploration of the phase space via forward deterministic simulations. We next show what can be obtained about the structural

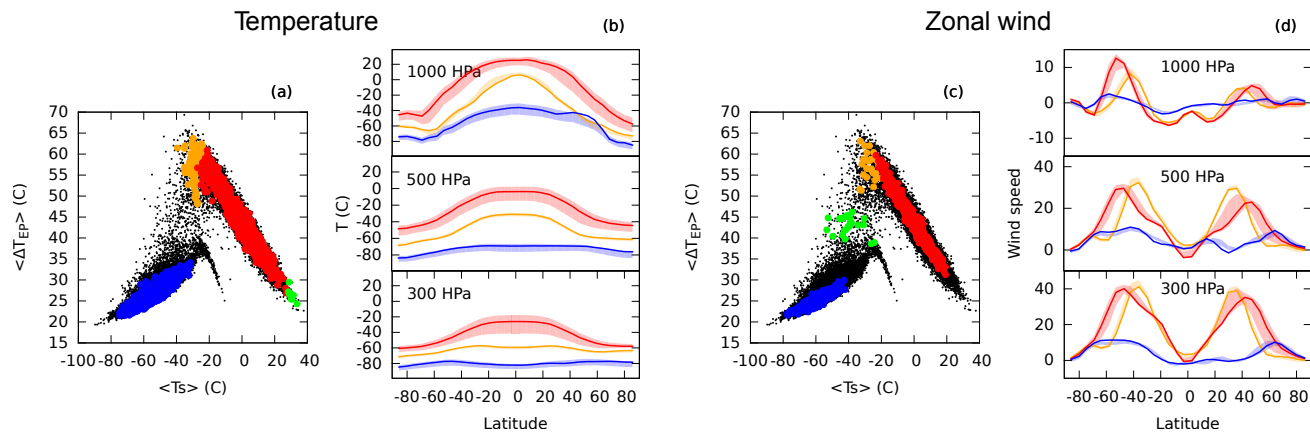


FIG. 12. The topography of the quasipotential in high-dimensional spaces. Panel (a) and (b): the analysis is performed for setup B and $\sigma = 12\%$ in the coordinate space of the temperatures at three different pressures (300, 500 and 1000 hPa) at 32 latitudes between -86° and 86° (96 variables). Panel (c) and (d): the analysis is performed on the time series of the zonal and the meridional wind in the same latitudes and pressures (192 variables). Panel (a) and (c) portray the estimated attractors of the quasipotential are represented in the plane of the 30-day averaged global temperature versus 30-day averaged Equator to pole temperature difference. The core sets of each attractor are colored in blue (SB state), orange (C state) and red (W state). The green points are the core set of spurious attractors found by the algorithms in both setups. The black points are configurations which do not belong to any core state. Panel (b) and (d) portray the average value plus/minus one standard deviation of the variables, restricted to the core sets of the SB (blue), W (red) and C (orange) states, as light shaded area. In comparison, the time averages of the same variables, computed for the corresponding deterministic attractors, is shown in dark solid lines of the same color, respectively. The meridional wind is not shown.

properties of the climate by treating the output of some given numerical simulations as pseudo-observations of an in principle unknown model, and applying a suite of data driven methods [62, 63, 65] presented in Section II B

We first consider a numerical integration of the model in setup B lasting $6 \cdot 10^4$ years and performed with $\sigma = 12\%$, the lowest value of noise considered in this work. From the complete trajectory of $O(10^5)$ d.o.f. recorded with having temporal resolution of one time step, we construct a severely coarse-grained version of the phase space by a set of monthly averaged temperatures measured every 10 months (hence, decimated with respect to the standard monthly averaged dataset) at three different pressures (300, 500 and 1000 hPa) and 32 different latitudes, for a total of 96 variables. The quasipotential as a function of these variables is, in principle, a 96-dimensional function, which cannot be visualized or estimated in a simple manner.

By using the approach outlined in Sec. II B, we study the topography of this function. We first estimate the intrinsic dimension of the manifold containing the data, which turns out to be ~ 11 , significantly smaller than the number of variables [115]. This number is approximately scale invariant: indeed the estimated value does not change significantly if the data set is significantly undersampled.

Since the intrinsic dimension of the embedding manifold is relatively low and well-defined, one can estimate the quasipotential Φ_t in each time frame t using Eq. (9), without defining explicitly the ~ 11 coordinates mapping the manifold. Using these estimates, one finds the attrac-

tors, which correspond to the local minima of Φ . With a statistical confidence level of 99 %, corresponding to $Z = 2.576$, we find 4 states, with a core population of 39171, 12099, 112 and 11 frames respectively. The configurations corresponding to the four minima of Φ were then evolved by a dynamics with $\sigma = 0$. While the first three evolve to the SB, W and C attractors, the fourth is unstable, and rapidly evolves to the W attractor. This indicates that the fourth state is an artifact of finite sampling, or of the variations of the $Z(x)$ (see Eq. (4)) which in the estimate of Φ_t are neglected. The configurations assigned to the core set of each of the three remaining states are represented in Fig. 12-a in the same projection used in Fig. 3. As already noticed, in this projection the C states is strongly overlapping with the W state, and no barrier is visible between the two.

In panel b we plot the average and the standard deviation, estimated for the core set of each state, of the 96 temperature variables used in the analysis. Note that such average values agree remarkably well with the time-averages one obtains by considering the corresponding deterministic attractors, represented as continuous lines in Figure 12. Remarkably, the distributions are significantly well separated for almost all the variables. This demonstrates that the W and C state, which are overlapping in the two-dimensional projection of panel a, are non-overlapping in the 96-dimensional space of these variables. This also shows that the data-driven approach presented here that feeds upon an individual trajectory of the stochastically perturbed system is able to reconstruct accurately the statistical properties of the compet-

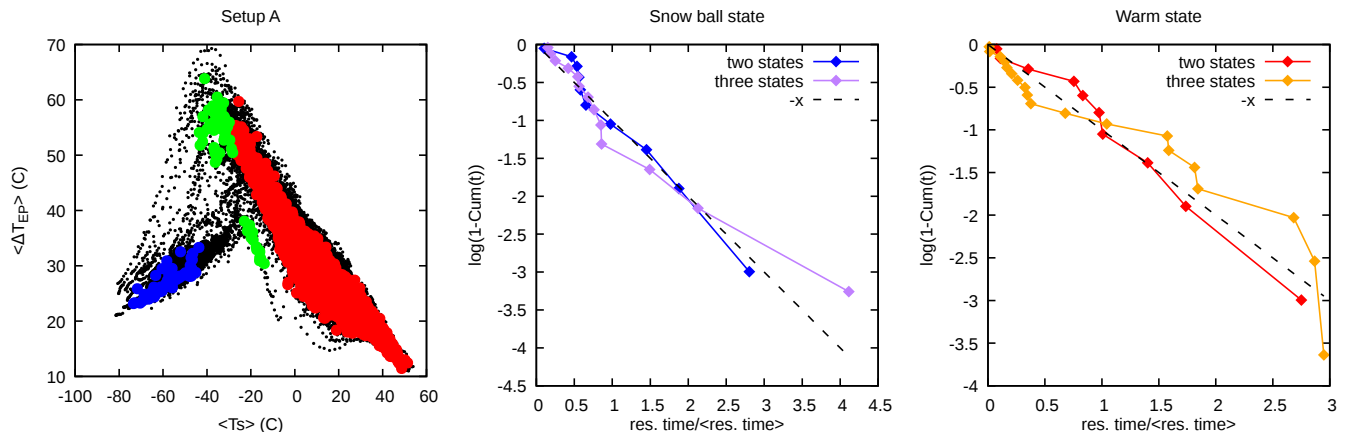


FIG. 13. The quasipotential and the residence times for setup A and $\sigma = 18\%$. Panel (a): the states obtained analyzing the coordinate space of the temperatures at three different pressures at 32 latitudes (the same variables used in the analysis in Fig. 12-a). The analysis is performed with $Z=5$. At higher statistical significance the green state disappears. Panel (b) and (c): the empirical cumulative distribution $C(x)$ of the normalized escape time $x = t_{esc} / \langle t_{esc} \rangle$, where $\langle t_{esc} \rangle$ is the average of all the observations. Panel (b): the SB state. Panel (c): the W state. Blue and red lines: the green state in panel a is not considered meaningful. Purple and orange lines: the green state is considered meaningful. The dashed black lines correspond to the ideal case in which $x \sim \exp(-x)$, and therefore $\log(1 - C(x)) = -x$.

ing deterministic metastable states. We then computed the quasipotential as a function of the 192 variables describing the wind direction and intensity at the same latitudes and pressures of the temperature variables. The intrinsic dimension of this dataset is ~ 16 , slightly larger than for the other variables. In this space, at a statistical confidence of 99% the algorithm is able to detect only two states, the W and the SB states. At a 98% confidence the C states appears (orange points in Fig. 12-c), together with another state, represented in green. The latter state turns out to be spurious, since a dynamics performed with $\sigma = 0$ started from the estimated minimum rapidly converges to the SB state. In this space the C state is much more similar to the W state, as illustrated in panel d: the average zonal wind differs significantly only at latitudes between $60^\circ S$ and $50^\circ S$, and not everywhere. Note also in this case the excellent agreement obtained with the average statistics computed for the corresponding deterministic attractors.

We also performed the same analysis on a simulation evolved for 32780 years using the model in setup A and with $\sigma = 18\%$. In this case, at high statistical significance, only two states are detected from the algorithm, the W and the SB states, consistently with the analysis described in Section IV B 1. However, at lower statistical significance other states appear. An example of an analysis is shown in Fig. 13-a, where the green state approximately occupies the region of the attractor C observed in setup B, in the two-dimensional projection used in Fig. 12-a. However, the multidimensional probability distribution of the temperature variables in this state differs significantly from the one of state C of setup B. Indeed this state is not an attractor: the configuration of lower Φ belonging to this state, if evolved with determin-

istic dynamics by setting $\sigma = 0$, converges rapidly to the W state. The dynamics of an ensemble of trajectories initiated near the green dots is by and large controlled by two subdominant eigenvectors depicted in Fig. 6a)-b).

These results indicate that our approach allows identifying the correct metastable states of a complex high-dimensional dynamic model, but these states come with an uncertainty, which partially derives from statistical errors, and partially from the approximations intrinsic in the quasipotential estimator, which neglects the pre-exponential factor $Z(x)$. Finally, an error is introduced by the correlation between the frames, which are generated by a dynamic model and sampled with a time lag of a few months. However, one can rather straightforwardly recognize the spurious states, even without performing a dynamics at $\sigma = 0$, by estimating, on the same trajectories which brings to their identification, the probability distribution of the first escape times. This distribution is estimated by assuming that the system performs a transition between two states when it visits a core configuration belonging to a state which is different from the state of the last core configuration visited in the past [116]. In this manner, one splits the trajectory in segments, each labeled with a different state, whose length is an estimate of the escape time t_{esc} . If the set of states defines (at least approximately) a Markov model, t_{esc} should be exponentially distributed. In figure 13-b and c we plot a function of the empirical cumulative probability distribution of t_{esc} which, if $t_{esc} \sim \text{Exp}$, should coincide with the black dashed lines. If one considers as meaningful also the green state in panel (a) one obtains a set of t_{esc} from the W and the SB state whose distribution significantly deviates from an exponential (purple and orange lines in panels b and c). If instead one does not consider

the green state as meaningful, the distribution of the escape times from the W and SB state is almost perfectly exponential (blue and red lines), as far as one can judge from the relatively small number of transition events observed in the trajectory. This analysis indicates that our approach allows identifying the *correct* metastable states of the system even from relatively short trajectories, in which only $\mathcal{O}(10)$ are observed. The states can be identified in a fully unsupervised manner, analyzing only the trajectory or by running short relaxation dynamics with $\sigma = 0$.

V. CONCLUSIONS

Achieving a deeper understanding of the nature of the Earth’s tipping points is one of the key contemporary challenges because it is essential for better framing the co-evolution of climatic conditions and of the biosphere throughout the Earth’s history, and, in the present context, for better constraining the current planetary boundaries through a careful examination of the safe operating space for Humanity [117]. Indeed, the most dangerous and harder-to-predict manifestations of the current climate *crisis* are associated with rapid and possibly irreversible changes in the tipping elements of the planet. This endeavour has, on top of enormous societal and environmental implications, great scientific relevance *per se* and can be framed as the investigation of multistability for an extremely complex system like our planet.

The framework we propose for investigating the multistability of the Earth system has similarities at formal level with proposals done in the context of evolutionary biology and boils down to a generalization of the classical and powerful idea of a stochastic dynamical system living in an energy landscape. The quasipotential is the function taking the role of the free energy in a more general context that include the case of nonequilibrium conditions. Local minima in the quasipotential describe competing metastable states, and are separated by local maxima and saddles – M states – that define possible gateways for transitions.

Such minima are arranged hierarchically and appear at multiple scales: large scale, deep local minima of the quasipotential landscape contain, if one looks carefully, many smaller-scale local minima, maxima, and saddles. We propose that this is a fundamental mathematical structure linking the global multistability of the climate system with the geographically localized tipping elements and the so-called cascading tipping points, and might be useful for understanding the associated multiscale hysteretic behaviour of the climate system when parameters are suitably modulated.

We foresee the possibility of interpreting and analysing the climate variability on ultralong, paleoclimatic time scales as itinerancy between possibly many competing metastable states, with proximity to M states defining times when the climate experienced sudden climatic

shifts. Some metastable states may be too shallow to be practically relevant compared to the intensity of the acting stochastic and/or deterministic forcing. Other metastable states might be just very far in the phase space and have never or will very likely never be visited. Transitions between metastable states might be facilitated by mechanisms like stochastic resonance [118], which has been recently reframed according to the formalism adopted here for treating nonequilibrium systems [119]. Indeed, stochastic resonance is thought to act in the climate system at different spatial and temporal scales, ranging from ultralong [120–122], to intermediate [123–126], to short ones [127–129].

The dynamics of the climate is here described through two versions of an open source climate model, PLASIM, which has an appropriate mix of precision, flexibility, and efficiency in simulating the present climate as well as very exotic climatic conditions. The first version (setup A) features a simplified but meaningful representation of the oceanic energy transport from low to high latitudes, whereas in the second one (setup B) large scale energy transport is provided solely by the turbulent atmosphere. Setup A demonstrates the well-known competing climatic states corresponding to the present warm (W) conditions and the so-called snowball (SB) climate. Setup B, instead, contains an unexpected additional intermediate stable climate (C) where the sea is partially ice-free in the equatorial band. The lack of a powerful mechanism of energy redistribution across the climate makes this additional state possible. The C state should not be regarded as a pure mathematical curiosity corresponding to a pathological solution: exotic climate states rather similar to the C state obtained here are deemed extremely relevant in paleoclimatic terms because they provide a scenario able to explain the survival of life during the Neoproterozoic glaciations.

Transitions between the competing basins of attraction are made possible when stochastic forcing – here in the form of a fluctuating solar irradiance – is introduced into the system. Indeed, many other sources of stochasticity are present in the real climate system. Moreover, in order to be able to explore the full phase space of the system within a reasonable time, we are compelled to consider a much stronger noise than what is deemed physically realistic for our planet, yet this has actually little impact on our main conclusions, because of the mathematical structure of the problem.

Indeed, we are able to compute the quasipotential function, which describes, on the one side, the invariant measure of the system and, on the other side, in its local version, controls the probability of transition of the stochastically forced trajectory from one to another basin of attraction. We are able to estimate in both setups the optimal escape paths – the instantons – and the corresponding relaxation trajectories linking the W and SB states, and are then able to verify the nonequivalence between the two, which is an essential feature of nonequilibrium properties.

Instantons describe how transitions take place in the zero-noise limit and are more of a mathematically elegant construction than a physically relevant object in our investigations, as we need to consider noise of moderate yet non-negligible intensity in order to observe reasonably frequent transitions between the SB and W attractors. Additionally, studying the transfer operator in a suitably projected space sheds light on how the system relaxes to its invariant measure. We are able to find clear evidence of both interwell relaxation processes, which describe transitions between competing metastable states, and are the noisy version of instantons, and intrawell relaxation processes, which would conventionally be labelled as ultralow frequency variability within the W state associated with large scale melting and thawing of sea ice and corresponding large temperature fluctuations.

A possibly nontrivial result we obtain is that the instantons escaping the SB and the W attractors do not meet at one of the M states separating the two corresponding basins of attraction. This can be best appreciated visually by watching the videos included in the SM. In fact, the transitions take place through two separate saddles, thereby implying the existence of large-scale nonvanishing currents in the phase space. This is a further, strong signature of the nonequilibrium equilibrium nature of the system, which can be captured also by looking at a severely projected Markov chain model. The existence of separate paths for the SB-to-W and W-to-SB states marks a relevant difference with previous studies. The presence of more evident macroscopic signature of nonequilibrium conditions can be attributed to the presence in this model of an active hydrological cycle, which is the major agent of entropy production in the climate system. The detection of the saddles using the classical edge tracking algorithm poses additional challenges compared to the standard case, because the dynamics on the basin boundary is, by itself, multistable.

The investigation of the properties of the C state in setup B clarifies the multiscale nature of multistability of the climate system. Indeed, such a state corresponds to a comparably shallower minimum of the quasipotential, which can be explored only considering significantly weaker noise than needed to explore globally the phase space of the system. We discover that the most natural, preferential escape route from the C state is towards the W state. The C state is only barely metastable, as even internally generated noise of the numerical discretization can destabilize it, even if only rarely and over ultra long time scales. The position in phase space of the C state and its properties indicate that it is likely that the C state is the leftover of the M state between the SB and W climate obtained as we progressively switch off the horizontal diffusivity of the ocean, because this leads to a less efficient redistribution of energy in the system,

We have complemented the top-down approach based on numerical modelling with data-driven methods – typically used in for studying molecular compounds – that allow for the automatic detection of the competing

metastable states from the analysis of single stochastic trajectory and to reconstruct the quasi-potential in arbitrarily high-dimension. The potential of this approach is outstanding, as we have been able to reconstruct the dynamical landscape of the climate model in both setups and gain a better understanding of how transitions between the competing metastables states occur. Additionally, by suitable averaging over many realizations, we have been able to reconstruct the climates of the competing (deterministic) metastable states.

We see the combination of the top-down and bottom-up approach as a possible way forward to study the multiscale nature of the multistability of the climate system, as well as of other systems of comparable complexity. This research work paves the way for further investigation into some fundamental properties of the climate system and goes in the direction of clarifying its intransitive vs quasitransitive vs transitive nature – in the sense of Lorenz [130] – when different time scales are considered. Additionally, it indicates a way for fostering the development of climate models of different level of complexity: indeed, we want them to be able to capture the qualitative features of climate, by allowing for the presence of a complex dynamical landscape featuring hierarchically arranged – according to the desired level of envisaged detail and granularity – metastable states.

The viewpoint presented here seems also extremely promising for investigating a separate, extremely relevant aspect of atmospheric dynamics, namely the existence in the atmosphere of different regimes of operation, which define the presence of substantial low-frequency variability on subseasonal time scales [4, 131]. This boils down to the fact that, at coarse-grained level, as a result of extremely dynamical heterogeneity [132], one is practically looking at a multistable system, where one can define and detect transitions between different metastable states [133].

Finally, we remark that white Gaussian noise might not necessarily be the only suitable way to treat stochasticity in the climate system [134]. The theory of escapes from attractors in the presence of Lévy noise has been developed [135, 136] and very recently applied to simple models of geophysical relevance [137]. It is well known that the mechanisms of escape are rather different than in the standard Gaussian scenario pursued in this paper. It seems then of great relevance to consider the effect of Lévy noise forcing in a more complex climate model like the one considered here.

ACKNOWLEDGMENTS

VL wishes to thank T. Bódai, N. Boers, M. Ghil, F. Lunkeit, G. Pavliotis, A. Tantet, and N. Zagli for many inspiring conversations on multistability and tipping points. GM wishes to thank F. Lunkeit for his guidance on PLASIM and kind hospitality at the University of Hamburg. TG acknowledges the support re-

ceived from the EPSRC project EP/T011866/1. VL acknowledges the support received from the EPSRC project EP/T018178/1. VL and GM acknowledge the support received from the EU Horizon 2020 project TiPES (Grant no. 820970).

Appendix A: Supplementary Material

1. Methods for Estimating the Transition Paths

The estimate of the average transitions path is performed as follows.

1. We first define a line – thin dashed black line in Fig. 4 – that clearly separates between the two metastable states;
2. We check whether a portion of the orbit, coming from a neighbourhood of the Ω_1 attractor, crosses the line, and eventually enters the neighbourhood of the attractor Ω_2 ;
3. If so, and the trajectory remained near Ω_1 for at least y years and then remains for Y years near Ω_2 , we store the $y + Y$ years long trajectory;
4. We perform a time average of the final set of trajectories.

To improve our estimate, we combine statistics from the simulations performed with the three smallest noise intensities $\% \sigma$, obtaining a set of roughly 100 $y + Y$ years long trajectories with the properties above. Here, for setup A it holds $y + Y = 2 + 14 = 16 \text{ yrs}$ for $SB \rightarrow W$ and $y + Y = 14 + 2 = 16 \text{ yrs}$ for $W \rightarrow SB$. For setup B it holds $y + Y = 4 + 36 = 40 \text{ yrs}$ for $SB \rightarrow W$ and $y + Y = 40 + 10 = 50 \text{ yrs}$ for $W \rightarrow SB$. Note that the results are robust both with respect to small changes in the choices of y , Y and of the geometry of the line used as a criterion for separating the two metastable states.

2. Relaxation trajectories

Figure 14 provides evidence for three stable climatic states, whose basin features are reported in Table I of the main paper. It shows the time evolution of $[\langle T_S \rangle]$, ΔT_{EP} , and sea ice percentage for three trajectories initialized in an unstable region of the phase space for setup B and undergoing a deterministic evolution with a constant value for $S^* = 1365 \text{ W/m}^2$, i.e. $\sigma = 0\%$. Accordingly, Fig. 15 shows the first 200 years of evolution of corresponding runs of Fig. 14 (a-b) in the reduced phase space projection $([\langle T_S \rangle], \Delta T_{EP})$ of the invariant measure.

3. Animations

We present here a series of animations that illustrate the real time dynamics of the climate model subjected to random yearly fluctuations of the solar constant S^* . To convey the dramatic implications of the global transitions taking place, we further present the corresponding daily evolution of four observables.

In the following, we focus in the cases where the system exhibits a noise induced transition among its basins of attraction. The layout of the animations is the same for consistency, and the frequency is 30 frames per second (fps), to match one month per second. The left part of the animations involves the projection of the quasipotential, shifted so that the global minimum is set to 0, on the reduced phase space spanned by the 30-day averaged global temperature $[\langle T_S \rangle]$, versus 30-day averaged Equator to pole temperature difference ΔT_{EP} for either setups (e.g. see Fig.4(b) of the paper). On top of this projection, the averaged transition path is overlaid following the steps described in Sec. A1. The interesting viewpoint is the real-time trajectory of the system in the $([\langle T_S \rangle], \Delta T_{EP})$ projected space, which is shown via the “snake-like” moving black line of 90-days long duration. Meanwhile, the box in the top right corner contains the month/year time-stamp together with the value of the solar constant for the particular year.

For the cases considered, unless otherwise stated, the real-time evolution is taken from the dataset with $\sigma = 20\%$ for setup A and $\sigma = 16\%$ for setup B [139]. Furthermore, as discussed in the paper, the transitions occur via two different channels indicating the existence of a current, which is a signature of nonequilibrium dynamics.

The right part of the animations gives an account of the corresponding temporal evolution of the distribution on Earth of four relevant climatic observables; namely, the surface temperature, the wind speed at 300 hPa, the Geopotential height at 500 hPa, and the sea ice cover. As the frequency is again 30 fps, slower playback speeds would help the interested viewer to observe finer details, if necessary. When contours are used, the colormap is adjusted to effectively show all the range of values that the system exhibits during its transition. Note that the choice of the particular observables also serves the purpose of showing the different and vast timescales within the system, with the winds having timescales of days, the Geopotential of weeks, the surface temperature of months and the sea-ice coverage of years.

Each animation is introduced via a snapshot below, which can be watched by clicking on the relevant link in the caption.

As discussed in the main paper, the key message of the following animations is that the forward and the corresponding backwards transition between two basins of attraction follow a different path in the phase space. This is a signature of enhanced nonequilibrium conditions, that can be attributed to the presence of an active hydrological cycle in the model. Furthermore, it also suggest a

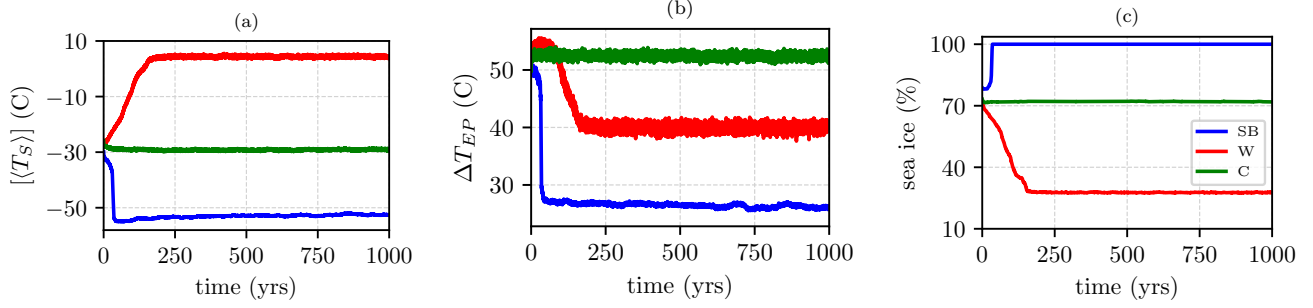


FIG. 14. Relaxation trajectories evolved in time as a function of 30-day averaged (a) global surface temperature (b) Equator to pole temperature difference and (c) sea ice percentage, using setup B, which clearly allows for the existence of three metastable climate states.

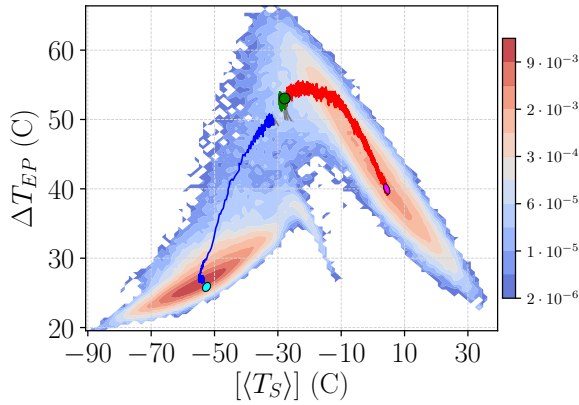


FIG. 15. The first 200 years of the relaxation trajectories of Fig. 14(a-b) in the reduced phase space projection ($\langle [T_S] \rangle$, ΔT_{EP}) of the invariant measure.

different route towards the thawing and freezing of the planet.

a. Setup A

For setup A we present two movies that portray the transition from the SB to the W state (Fig. 16) and from the W to the SB state (Fig. 17). The mean escape paths are included as a red (blue) line towards the W (SB) attractor.

b. Setup B

For setup B we present a more extended set of movies, in order to better capture the higher complexity of the dynamical landscape of this version of the model. Figures 18 and 19 give access to the movies that portray the direct transition from the SB to the W state and from the W to the SB state, respectively. Instead, from Figs. 20 and 21 we can access the movies portraying a transition

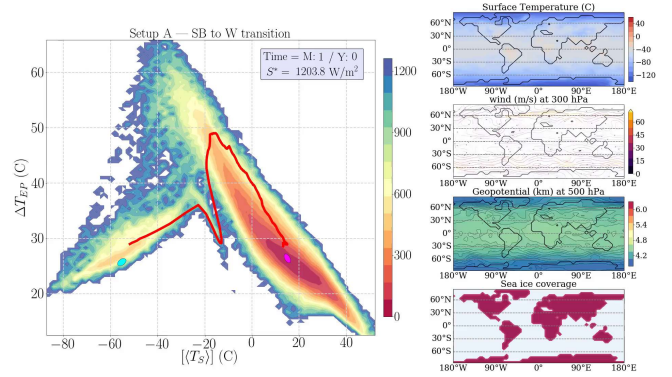


FIG. 16. Setup A: Snowball to Warm transition. Click for video

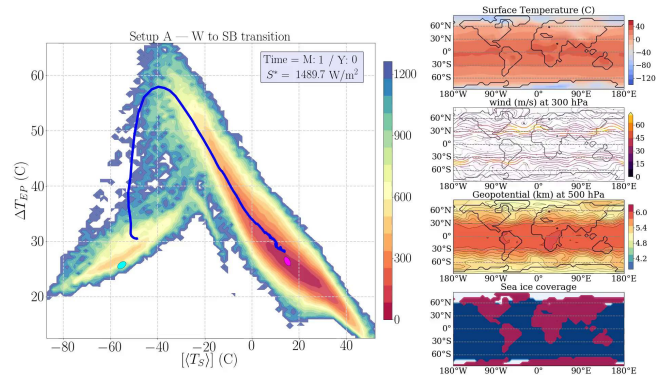


FIG. 17. Setup A: Warm to Snowball transition. Click for video

from the SB to the W state and from the W to the SB state, respectively, that feature the C state as intermediate step. The mean direct escape paths are included as a red (blue) line towards the W (SB) attractor.

a. Noise induced transitions from C state In these animations we start from C state and then impose a much weaker noise, $\sigma = 6\%$ to perturb it and induce a transition towards either the W (Fig. 22) or the SB (Fig. 23) basin of attraction. The mean escape paths are included

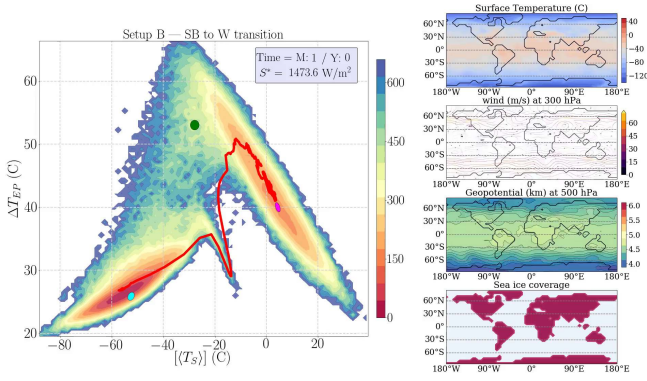


FIG. 18. Setup B: Snowball to Warm transition. Click for video

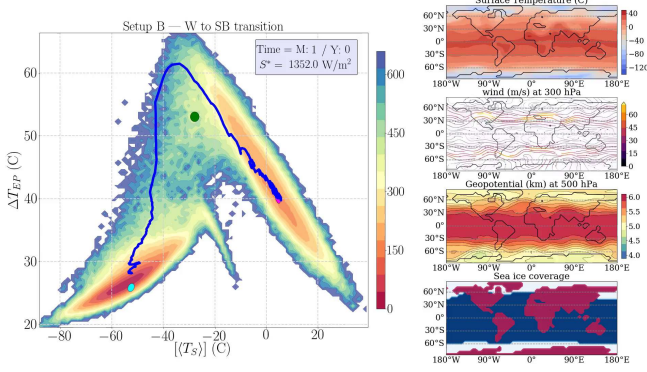


FIG. 19. Setup B: Warm to Snowball transition. Click for video

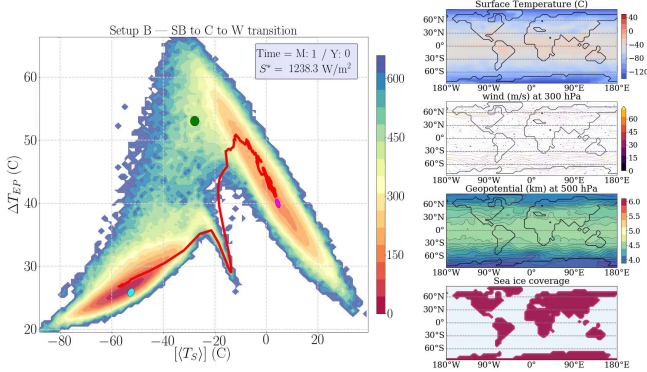


FIG. 20. Setup B: Snowball to Cold to Warm transition. In this example the system starting from the SB basin of attraction spends a few years in the C basin of attraction before transitioning towards the W basin of attraction. This dataset is taken from $\sigma = 12\%$ for setup B [139]. Click for video

as a red (blue) line towards the W (SB) attractor.

b. Remark on the C state We would like to add a final remark regarding the numerical stability of the C state, as in a quite rare occasion, we observed a $C \rightarrow W$ transition with $\sigma = 0$ of only one out of many relaxation trajectories, after evolving it for roughly 4000 years.

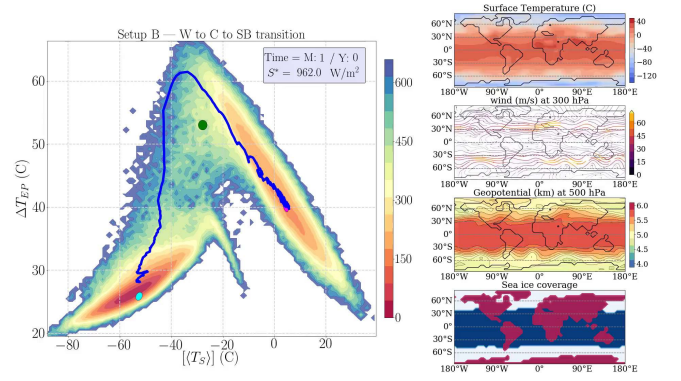


FIG. 21. Setup B: Warm to Cold to Snowball transition. In this example the system starting from the W basin of attraction spends a few years in the C basin of attraction before transitioning towards the SB basin of attraction. Click for video

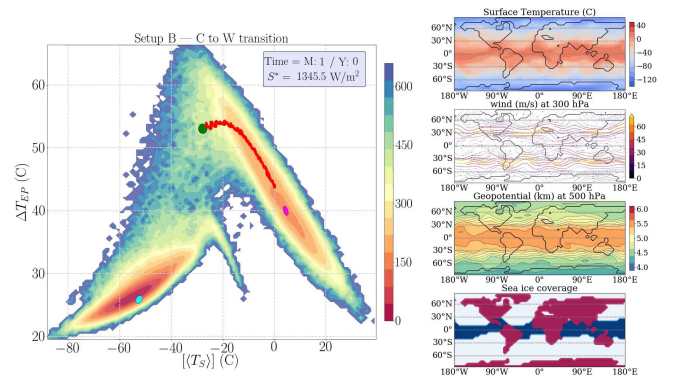


FIG. 22. Setup B: Cold to Warm transition. Click for video

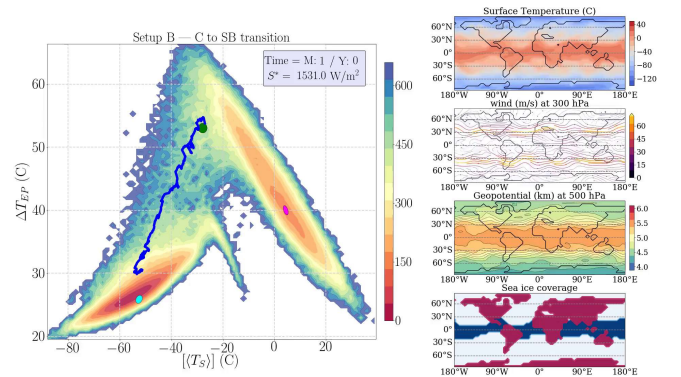


FIG. 23. Setup B: Cold to Snowball transition. Click for video

Tracing back on the cause behind this, we identified a source of intrinsic noise in our model, related to the sea-ice module. In particular, we observed that, very rarely, certain oceanic grid points would abruptly “flicker” between presence or absence of sea-ice on a day-to-day basis. Note that PLASIM allows only a binary state for sea-ice, thus effectively introducing a truncation noise. Switching from sea-ice to open sea has dramatic con-

sequences in the local energy budget, because the surface albedo goes from very high to very low. In some cases, such flickering would permanently change the status of nearby grid points, thus triggering a gradual long term elimination of the sea-ice coverage. Once a certain threshold was passed, a rapid transition to the W state was observed. The phenomenology of this numerical artifact indeed agrees with the very low $C \rightarrow W$ barrier we estimated.

4. Transfer Operator and Finite State Markov Representation

The transfer operator semigroup $\{\mathcal{L}^t\}_{t \geq 0}$ corresponding to the SDE given in Eq. (3) of the main text can be defined as the solution of the Fokker-Planck Equation [138]:

$$\begin{aligned} \partial_t \rho(\mathbf{x}, t) &= \mathcal{A}\rho(\mathbf{x}, t) := -\nabla \cdot (\mathbf{F}\rho(\mathbf{x}, t)) \\ &\quad + \frac{\sigma^2}{2} \sum_{i,j=1}^N \partial_{x_i, x_j} C(\mathbf{x}) \rho(\mathbf{x}, t). \end{aligned} \quad (\text{A1})$$

where $\rho(\mathbf{x}, t) = \mathcal{L}^t \rho_0(\mathbf{x})$ for some initial condition $\rho_0 \in L^1(X)$, and $\mathcal{L}^t = \exp(At)$. The transfer operator \mathcal{L}^t describes the pushforward of an integrable function under the action of the dynamical system for a time duration of t . It turns out that \mathcal{L}^t is a contraction and the set $\{\mathcal{L}^t\}_{t \geq 0}$ is a C_0 -semigroup, so that $\mathcal{L}^{t_1+t_2} = \mathcal{L}^{t_1} \mathcal{L}^{t_2} \forall t_1, t_2 \geq 0$. The differential operator \mathcal{A} is the generator of the C_0 -semigroup. The invariant measure is the eigenvector with eigenvalue 0 of the operator \mathcal{A} : $\mathcal{A}\rho_\sigma(\mathbf{x}) = 0$ and can be normalised to one. The other eigenvectors of \mathcal{A} integrate to zero and their corresponding eigenvalues have real part that is strictly smaller than zero if we assume that the system is mixing. The subdominant eigenvalue with largest real part controls the speed of convergence of an arbitrary initial measure to the invariant one.

Typically, in many applications one needs to construct finite-state approximation of the phase space. We refer the reader to [50] for a detailed treatment of what follows below. To do this, we shall consider a finite shape-regular partition phase-space X into M regions or *boxes* $\{B_i\}_{i=1}^M$ and define $\mathbf{1}_{B_i}$ as the characteristic function on box $B_i \subset X$. Thus, we define the projection $P_M : L^1(X) \rightarrow U_M := \text{Span}(\{\mathbf{1}_{B_i}\}_{i=1}^M)$ as

$$P_M f = \sum_{i=1}^M \mathbf{1}_{B_i} \frac{\langle f \mathbf{1}_{B_i} \rangle_{\rho_\sigma}}{\langle \mathbf{1}_{B_i} \rangle_{\rho_\sigma}} \quad (\text{A2})$$

where $\langle g \rangle_{\rho_\sigma} = \int \rho_\sigma(\mathbf{x}) g(\mathbf{x}) d\mathbf{x}$. It follows that the operator $P_M \mathcal{L}^t : U_M \rightarrow U_M$ admits a matrix representation:

$$\mathcal{M}_{i,j}^t := (P_M \mathcal{L}^t)_{i,j} = \frac{\langle \mathbf{1}_{B_j} \mathcal{L}^t \mathbf{1}_{B_i} \rangle_{\rho_\sigma}}{\langle \mathbf{1}_{B_j} \rangle_{\rho_\sigma}}, \quad (\text{A3})$$

which happens to be a Markov or *stochastic* matrix, so that $\sum_{j=1}^M \mathcal{M}_{i,j} = 1$, $\mathcal{M}_{i,j} \geq 0$. The finite-state approximation to the invariant measure is obtained as $\lambda = 1$ solution to the eigenvalue problem $\mathcal{M}\mathbf{u} = \lambda\mathbf{u}$.

For high-dimensional systems – say with $N \gg 3$ – one is led to study the evolution of densities in a reduced space (the two-dimensional space $([T_S], \Delta T_{EP})$ in the examples above). The procedure we follow goes through the following steps: 1) we discretize the transfer reduced operator on a finite family of basis functions in the projected space; 2) we estimate the transition probabilities in a frequentist way from a long time series. Unfortunately, the dynamics in the reduced space is non-Markovian, as clarified by the classical results by Mori and Zwanzig. As a result, the semigroup property of the transfer operator is in general lost for the projected operator:

$\mathcal{M}_{i,j}^{t_1+t_2} = (P_M(\mathcal{L}^{t_1+t_2}))_{i,j} = (P_M(\mathcal{L}^{t_1} \mathcal{L}^{t_2}))_{i,j} \neq (P_M(\mathcal{L}^{t_1}))_{i,k} (P_M(\mathcal{L}^{t_2}))_{k,j}$, and the identification of the first subdominant eigenvectors and eigenvalues of \mathcal{M}^τ with the slowest decaying modes and their decay over a time scale of τ is only tentative. Nonetheless, by making a reasonable choice of τ and by considering observables that have a relevant projection on the reaction coordinates of the system and given an important contribution to the slow dynamical processes (in our case the ice-albedo and the radiative feedback and the large scale energy transports), one expects to find results that have at least qualitative relevance, as shown in Figs. 6 and 12 of the main text.

5. Remark on the intrinsic dimension

We include here a further supporting remark on the estimation of the intrinsic dimension (ID) of the manifold containing the data. It follows the approach described in [62], where the number of points in abscissas is selected at random. In Fig. 24 the error bars are the standard deviation of the ID estimated over different samples of the same size.

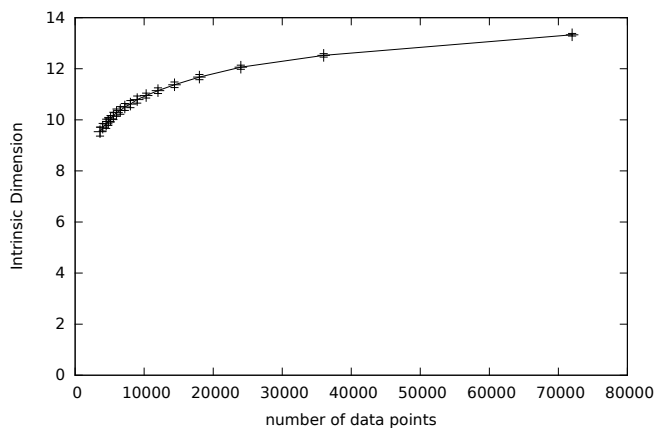


FIG. 24. The intrinsic dimension estimated for the data set analyzed in Fig 12, a trajectory of setup B and $\sigma = 12\%$ in the coordinate space of the temperatures at three different pressures (300, 500 and 1000 hPa) at 32 latitudes between -86° and 86° (a total of 96 variables).

6. Data Availability

We provide the data required to generate the figures of the main paper via a CC BY 4.0 license in [139]. Within these files further instructions and information is given to allow the interested reader to either directly repro-

duce the figures, or others are the raw data one needs to reproduce the figures using the methodologies described in the paper. The videos are publicly available on the [youtube.com](https://www.youtube.com) platform through the provided links and can be freely downloaded from there.

-
- [1] J. P. Peixoto and A. H. Oort, *Physics of Climate* (AIP Press, New York, New York, 1992).
- [2] V. Lucarini, R. Blender, C. Herbert, F. Ragone, S. Pascale, and J. Wouters, *Rev. Geophys.* **52**, 809 (2014a).
- [3] M. Ghil, in *Climate Change : Multidecadal and Beyond*, edited by C. C. P., G. M., L. M., and W. J. M. (World Scientific Publishing Co./Imperial College Press, 2015) pp. 31–51.
- [4] M. Ghil and V. Lucarini, *Rev. Mod. Phys.* **92**, 035002 (2020).
- [5] S. H. Schneider and R. E. Dickinson, *Reviews of Geophysics* **12**, 447 (1974).
- [6] B. Saltzman, *Dynamical Paleoclimatology: Generalized Theory of Global Climate Change* (Academic Press New York, New York, 2001).
- [7] I. M. Held, *Bulletin of the American Meteorological Society* **86**, 1609 (2005).
- [8] V. Lucarini, in *Models, Simulations, and the Reduction of Complexity*, edited by U. Gohde, S. Hartmann, and J. Wolf (De Gruyter, 2013) pp. 229–254.
- [9] M. I. Budyko, *Tellus* **21**, 611 (1969), <https://doi.org/10.3402/tellusa.v21i5.10109>.
- [10] W. D. Sellers, *Journal of Applied Meteorology* **8**, 392 (1969).
- [11] M. Ghil, *Journal of the Atmospheric Sciences* **33**, 3 (1976), [https://journals.ametsoc.org/jas/article-pdf/33/1/3/3419240/1520-0469\(1976\)033-0003_csfast_2.0_co.2.pdf](https://journals.ametsoc.org/jas/article-pdf/33/1/3/3419240/1520-0469(1976)033-0003_csfast_2.0_co.2.pdf).
- [12] H. Stommel, *Tellus* **2**, 244 (1961).
- [13] G. Veronis, *J. Atmos. Sci.* **20**, 577 (1963).
- [14] C. Rooth, *Progress in Oceanography* **11**, 131 (1982).
- [15] J. G. Charney and J. G. DeVore, *J. Atmos. Sci.* **36**, 1205 (1979).
- [16] E. N. Lorenz, *Tellus A: Dynamic Meteorology and Oceanography* **36**, 98 (1984).
- [17] E. N. Lorenz, in *Predictability of Weather and Climate*, edited by T. Palmer and R. Hagedorn (Cambridge University Press, 1996) pp. 40–58.
- [18] J. Marshall and F. Molteni, *Journal of the Atmospheric Sciences* **50**, 1792 (1993), [https://journals.ametsoc.org/jas/article-pdf/50/12/1792/3426388/1520-0469\(1993\)050-1792_taduop_2.0_co.2.pdf](https://journals.ametsoc.org/jas/article-pdf/50/12/1792/3426388/1520-0469(1993)050-1792_taduop_2.0_co.2.pdf).
- [19] K. Fraedrich, E. Kirk, and F. Lunkeit, Technical Report 16 Deutsches Klimarechenzentrum (1998).
- [20] V. Petoukhov, A. Ganopolski, V. Brovkin, M. Claussen, A. Eliseev, C. Kubatzki, and S. Rahmstorf, *Climate Dynamics* **16**, 1 (2000).
- [21] M. Montoya, A. Griesel, A. Levermann, J. Mignot, M. Hofmann, A. Ganopolski, and S. Rahmstorf, *Climate Dynamics* **25**, 237 (2005).
- [22] T. F. Stocker, D. Qin, G.-K. Plattner, M. Tignor, S. K. Allen, J. Boschung, A. Nauels, Y. Xia, V. Bex, P. M. Midgley, *et al.*, Contribution of working group I to the fifth assessment report of the intergovernmental panel on climate change **1535** (2013).
- [23] D. A. Randall, ed., *General Circulation Model Development: Past, Present and Future* (Academic Press, New York, 2000).
- [24] J. Berner, U. Achatz, L. Batté, L. Bengtsson, A. d. I. Cámara, H. M. Christensen, M. Colangeli, D. R. B. Coleman, D. Crommelin, S. I. Dolaptchiev, C. L. E. Franzke, P. Friederichs, P. Imkeller, H. Järvinen, S. Juricke, V. Kitsios, F. Lott, V. Lucarini, S. Mahajan, T. N. Palmer, C. Penland, M. Sakradzija, J.-S. von Storch, A. Weisheimer, M. Weniger, P. D. Williams, and J.-I. Yano, *Bulletin of the American Meteorological Society* **98**, 565 (2017), <https://doi.org/10.1175/BAMS-D-15-00268.1>.
- [25] T. M. Lenton, H. Held, E. Kriegler, J. W. Hall, W. Lucht, S. Rahmstorf, and H. J. Schellnhuber, *Proceedings of the national Academy of Sciences* **105**, 1786 (2008).
- [26] N. Boers, N. Marwan, H. M. J. Barbosa, and J. Kurths, *Scientific Reports* **7**, 41489 (2017).
- [27] S. Rahmstorf, M. Crucifix, A. Ganopolski, H. Goosse, I. Kamenkovich, R. Knutti, G. Lohmann, R. Marsh, L. A. Mysak, Z. Wang, and A. J. Weaver, *Geophysical Research Letters* **32** (2005), 10.1029/2005GL023655.
- [28] K. M. Walter, S. A. Zimov, J. P. Chanton, D. Verbyla, and F. S. Chapin, *Nature* **443**, 71 (2006).
- [29] A. Levermann, J. Schewe, V. Petoukhov, and H. Held, *Proceedings of the National Academy of Sciences* **106**, 20572 (2009), <https://www.pnas.org/content/106/49/20572.full.pdf>.
- [30] W. Steffen, J. Rockström, K. Richardson, T. M. Lenton, C. Folke, D. Liverman, C. P. Summerhayes, A. D. Barnosky, S. E. Cornell, M. Crucifix, J. F. Donges, I. Fetzer, S. J. Lade, M. Scheffer, R. Winkelmann, and H. J. Schellnhuber, *Proceedings of the National Academy of Sciences* **115**, 8252 (2018), <https://www.pnas.org/content/115/33/8252.full.pdf>.
- [31] A. K. Klose, V. Karle, R. Winkelmann, and J. F. Donges, *Royal Society Open Science* **7**, 200599 (2020), <https://royalsocietypublishing.org/doi/pdf/10.1098/rsos.200599>.
- [32] V. Lucarini, K. Fraedrich, and F. Lunkeit, *Quarterly Journal of the Royal Meteorological Society* **136**, 2 (2010), <https://rmets.onlinelibrary.wiley.com/doi/pdf/10.1002/qj.543>.
- [33] V. Lucarini and T. Bódai, *Nonlinearity* **30**, R32 (2017).
- [34] R. Pierrehumbert, D. Abbot, A. Voigt, and D. Koll, *Annual Review of Earth and Planetary Sciences* **39**, 417 (2011), <https://doi.org/10.1146/annurev-earth-040809-152447>.
- [35] P. F. Hoffman, A. J. Kaufman, G. P. Halverson, and D. P. Schrag, *Science* **281**, 1342 (1998),

- <https://science.sciencemag.org/content/281/5381/1342.full.pdf>
- [36] M. Brunetti, J. Kasparian, and C. V erard, *Climate Dynamics* **53**, 6293 (2019).
- [37] V. Lucarini and T. B odai, *Nonlinearity* **33**, R59 (2020).
- [38] S. J. Gould, *Wonderful Life: The Burgess shale and the Nature of History* (W.W. Norton, New York, 1989).
- [39] S. Morris, *The Crucible of Creation: The Burgess Shale and the Rise of Animals*, Popular science (Oxford University Press, Oxford, 1998).
- [40] C. Waddington and H. Kacser, *The Strategy of the Genes: A Discussion of Some Aspects of Theoretical Biology* (Allen & Unwin, 1957).
- [41] P. Ao, *Journal of Genetics and Genomics* **36**, 63 (2009).
- [42] J. E. Ferrell, *Curr. Biol.* **22**, R458 (2012).
- [43] S. Huang, *BioEssays* **34**, 149 (2012).
- [44] R. H. H. Janssen, M. B. J. Meinders, E. H. Van Nes, and M. Scheffer, *Global Change Biology* **14**, 1104 (2008), <https://onlinelibrary.wiley.com/doi/pdf/10.1111/j.1365-2486.2008.01540.x>.
- [45] V. Lembo, V. Lucarini, and F. Ragone, *Scientific Reports* **10**, 8668 (2020).
- [46] V. Lucarini, F. Ragone, and F. Lunkeit, *Journal of Statistical Physics* **166**, 1036 (2017).
- [47] O. Butterley and C. Liverani, *Journal of Modern Dynamics* **1**, 301 (2007).
- [48] V. Lucarini, *Journal of Statistical Physics* **162**, 312 (2016).
- [49] M. D. Chekroun, D. J. Neelin, D. Kondrashov, M. J. C., and M. Ghil, *Proceedings of the National Academy of Sciences* **111**, 1684 (2014).
- [50] A. Tantet, V. Lucarini, F. Lunkeit, and H. A. Dijkstra, *Nonlinearity* **31**, 2221 (2018).
- [51] K. Fraedrich, H. Jansen, E. Kirk, U. Luksch, and F. Lunkeit, *Meteorologische Zeitschrift* **14**, 299 (2005).
- [52] V. Lucarini, K. Fraedrich, and F. Lunkeit, *Atmospheric Chemistry and Physics* **10**, 9729 (2010).
- [53] R. Boschi, V. Lucarini, and S. Pascale, *Icarus* **226**, 1724 (2013).
- [54] P. B. Holden, N. Edwards, K. Fraedrich, E. Kirk, F. Lunkeit, and X. Zhu, *Geoscientific Model Development* **9**, 3347 (2016).
- [55] F. Ragone, V. Lucarini, and F. Lunkeit, *Climate Dynamics* **46**, 1459 (2016).
- [56] P. B. Holden, N. R. Edwards, T. F. Rangel, E. B. Pereira, G. T. Tran, and R. D. Wilkinson, *Geoscientific Model Development* **12**, 5137 (2019).
- [57] V. Lucarini and T. B odai, *Phys. Rev. Lett.* **122**, 158701 (2019).
- [58] R. Graham, in *Fluctuations and Stochastic Phenomena in Condensed Matter* (Springer, 1987) pp. 1–34.
- [59] A. Hamm, T. T el, and R. Graham, *Physics Letters A* **185**, 313 (1994).
- [60] J. X. Zhou, M. D. S. Aliyu, E. Aurell, and S. Huang, *Journal of The Royal Society Interface* **9**, 3539 (2012), <https://royalsocietypublishing.org/doi/pdf/10.1098/rsif.2012.0934>.
- [61] P. Zhou and T. Li, *The Journal of Chemical Physics* **144**, 094109 (2016), <https://doi.org/10.1063/1.4943096>.
- [62] E. Facco, M. d’Errico, A. Rodriguez, and A. Laio, *Scientific reports* **7**, 12140 (2017).
- [63] A. Rodriguez, M. d’Errico, E. Facco, and A. Laio, *Journal of chemical theory and computation* **14**, 1206 (2018).
- [64] M. d’Errico, E. Facco, A. Laio, and A. Rodriguez, *arXiv preprint arXiv:1802.10549* (2018).
- [65] A. Rodriguez and A. Laio, *Science* **344**, 1492 (2014).
- [66] A. Tantet, F. R. van der Burgt, and H. A. Dijkstra, *Chaos: An Interdisciplinary Journal of Nonlinear Science* **25**, 036406 (2015).
- [67] M. Santos Guti errez and V. Lucarini, *Journal of Statistical Physics* (2020), 10.1007/s10955-020-02504-4.
- [68] J. P. Lewis, A. J. Weaver, and M. Eby, *Journal of Geophysical Research: Oceans* **112** (2007), 10.1029/2006JC004037, <https://agupubs.onlinelibrary.wiley.com/doi/pdf/10.1029/2006JC004037>.
- [69] D. S. Abbot, A. Voigt, and D. Koll, *Journal of Geophysical Research: Atmospheres* **116** (2011), 10.1029/2011JD015927, <https://agupubs.onlinelibrary.wiley.com/doi/pdf/10.1029/2011JD015927>.
- [70] C. Grebogi, E. Ott, and J. A. Yorke, *Phys. Rev. Lett.* **50**, 935 (1983).
- [71] J. Vollmer, T. M. Schneider, and B. Eckhardt, *New Journal of Physics* **11**, 013040 (2009).
- [72] Y.-C. Lai and T. T el, *Transient chaos: complex dynamics on finite time scales*, Vol. 173 (Springer Science & Business Media, 2011).
- [73] J. D. Skufca, J. A. Yorke, and B. Eckhardt, *Physical Review Letters* **96**, 174101 (2006).
- [74] T. B odai, V. Lucarini, F. Lunkeit, and R. Boschi, *Climate Dynamics* **44**, 3361 (2015).
- [75] P. Ashwin, S. Wicczorek, R. Vitolo, and P. Cox, *Philosophical Transactions of the Royal Society A: Mathematical, Physical and Engineering Sciences* **370**, 1166 (2012), <https://royalsocietypublishing.org/doi/pdf/10.1098/rsta.2011.0306>.
- [76] P. H anggi, *Journal of Statistical Physics* **42**, 105 (1986).
- [77] P. Grassberger, *Journal of Physics A: Mathematical and General* **22**, 3283 (1989).
- [78] M. I. Freidlin and A. D. Wentzell, *Random perturbations of dynamical systems* (Springer, New York, 1984).
- [79] K. Hasselmann, *Tellus* **28**, 473 (1976).
- [80] Imkeller, P. and von Storch, J.S., *Stochastic Climate Models* (Birkhauser, Basel, 2001).
- [81] A. J. Majda, I. Timofeyev, and E. Vanden Eijnden, *Communications on Pure and Applied Mathematics* **54**, 891 (2001), <https://onlinelibrary.wiley.com/doi/pdf/10.1002/cpa.1014>.
- [82] D. R. Bell, in *Real and stochastic analysis* (Springer, 2004) pp. 9–42.
- [83] R. Graham, A. Hamm, and T. T el, *Phys. Rev. Lett.* **66**, 3089 (1991).
- [84] P. Gaspard, *Journal of statistical physics* **106**, 57 (2002).
- [85] F. Bouchet, K. Gawedzki, and C. Nardini, *Journal of Statistical Physics* **163**, 1157 (2016).
- [86] P. Ao, *Journal of Physics A: Mathematical and General* **37**, L25 (2004).
- [87] R. Yuan, Y. Tang, and P. Ao, *Frontiers of Physics* **12**, 120201 (2017).
- [88] R. Kautz, *Physics Letters A* **125**, 315 (1987).
- [89] T. Grafke, R. Grauer, and T. Sch afer, *Journal of Physics A: Mathematical and Theoretical* **48**, 333001 (2015).
- [90] T. Grafke, *Journal of Statistical Mechanics: Theory and Experiment* **2019**, 043206 (2019).
- [91] H. A. Kramers, *Physica* **7**, 284 (1940).
- [92] P. Grassberger and I. Procaccia, *The Theory of Chaotic Attractors*, , 170 (2004).
- [93] P. Frederickson, J. L. Kaplan, E. D. Yorke, and J. A. Yorke, *Journal of Differential Equations* **49**, 185 (1983).

- [94] V. Lucarini, D. Faranda, A. C. G. M. M. de Freitas, J. M. M. de Freitas, M. Holland, T. Kuna, M. Nicol, M. Todd, and S. Vaienti, *Extremes and Recurrence in Dynamical Systems* (Wiley, New York, 2016).
- [95] D. Faranda, G. Messori, and P. Yiou, *Scientific Reports* **7**, 41278 (2017).
- [96] Y. Mack and M. Rosenblatt, *Journal of Multivariate Analysis* **9**, 1 (1979).
- [97] V. Eyring, S. Bony, G. A. Meehl, C. A. Senior, B. Stevens, R. J. Stouffer, and K. E. Taylor, *Geoscientific Model Development* **9**, 10539 (2016).
- [98] S. A. Orszag, *Journal of the Atmospheric Sciences* **27**, 890 (1970).
- [99] G. J. Haltiner and R. T. Williams, *Numerical prediction and dynamic meteorology* (John Wiley and Sons, New York, 1982).
- [100] J. Semtner, Albert J., *Journal of Physical Oceanography* **6**, 379 (1976).
- [101] H. A. Dijkstra and M. Ghil, *Reviews of Geophysics* **43**, RG3002 (2005).
- [102] T. Kuhlbrodt, A. Griesel, M. Montoya, A. Levermann, M. Hofmann, and S. Rahmstorf, *Reviews of Geophysics* **45** (2007), 10.1029/2004RG000166.
- [103] P. Cessi, *Annual Review of Marine Science* **11**, 249 (2019).
- [104] K. E. Trenberth, J. T. Fasullo, and J. Kiehl, *Bulletin of the American Meteorological Society* **90**, 311 (2009).
- [105] V. Lucarini and F. Ragone, *Rev. Geophys.* **49**, RG1001 (2011).
- [106] M.-A. Knietzsch, A. Schröder, V. Lucarini, and F. Lunkeit, *Earth System Dynamics* **6**, 591 (2015).
- [107] E. N. Lorenz and F. N. Lorenz, *The nature and theory of the general circulation of the atmosphere*, Vol. 218 (World Meteorological Organization Geneva, 1967).
- [108] O. Pauluis and I. M. Held, *J. Atmos. Sci.* **59**, 140 (2002).
- [109] V. Lucarini, *Physical Review E* **80**, 021118 (2009).
- [110] R. Goody, *Q. J. R. Meteorol. Soc.* **126**, 1953 (2000).
- [111] V. Lucarini and S. Pascale, *Climate Dynamics* **43**, 981 (2014).
- [112] P. Gaspard, *Journal of Statistical Physics* **117**, 599 (2004).
- [113] M. Linsenmeier, S. Pascale, and V. Lucarini, *Planetary and Space Science* **105**, 43 (2015).
- [114] W. T. Hyde, T. J. Crowley, S. K. Baum, and W. R. Peltier, *Nature* **405**, 425 (2000).
- [115] Note that we should not in any way interpret this number as representative of the actual effective dimension of the attractor of the climate system, because the coarse graining procedure applied in space and time filters out almost entirely the dynamics – which is prevalent in this climate model as well as in reality – occurring over time scales shorter than one seasons and featuring longitudinally symmetric structure [4].
- [116] C. Schütte, F. Noé, J. Lu, M. Sarich, and E. Vandeneijnden, *The Journal of chemical physics* **134**, 05B609 (2011).
- [117] J. Rockström, W. Steffen, K. Noone, Å. Persson, F. S. Chapin, E. F. Lambin, T. M. Lenton, M. Scheffer, C. Folke, H. J. Schellnhuber, B. Nykvist, C. A. de Wit, T. Hughes, S. van der Leeuw, H. Rodhe, S. Sörlin, P. K. Snyder, R. Costanza, U. Svedin, M. Falkenmark, L. Karlberg, R. W. Corell, V. J. Fabry, J. Hansen, B. Walker, D. Liverman, K. Richardson, P. Crutzen, and J. A. Foley, *Nature* **461**, 472 (2009).
- [118] L. Gammaitoni, P. Hänggi, P. Jung, and F. Marchesoni, *Reviews of Modern Physics* **70**, 223 (1998).
- [119] V. Lucarini, *Phys. Rev. E* **100**, 062124 (2019).
- [120] R. Benzi, A. Sutera, and A. Vulpiani, *Journal of Physics A: Mathematical and General* **14**, L453 (1981).
- [121] C. Nicolis, *Tellus* **34**, 308 (1982), <https://doi.org/10.3402/tellusa.v34i3.10817>.
- [122] P. D. Ditlevsen, *Chemical Physics* **375**, 403 (2010).
- [123] R. B. Alley, S. Anandakrishnan, and P. Jung, *Paleoceanography* **16**, 190 (2001), <https://agupubs.onlinelibrary.wiley.com/doi/pdf/10.1029/2000PA0038501> (2002).
- [125] P. Vélez-Belchí, A. Alvarez, P. Colet, J. Tintore, and R. L. Haney, *Geophys. Res. Lett.* **28**, 2053 (2001).
- [126] V. Lucarini, D. Faranda, and M. Willeit, *Nonlinear Processes in Geophysics* **19**, 9 (2012).
- [127] Q. Han, T. Yang, C. Zeng, H. Wang, Z. Liu, Y. Fu, C. Zhang, and D. Tian, *Physica A: Statistical Mechanics and its Applications* **408**, 96 (2014).
- [128] Z.-L. Jia, C.-Y. Yang, C. Li, and D.-C. Mei, *Journal of Statistical Mechanics: Theory and Experiment* **2014** (2014), 10.1088/1742-5468/2014/03/P03022.
- [129] K.-K. Wang, Y.-J. Wang, and J.-C. Wu, *Modern Physics Letters B* **30**, 1650308 (2016), <https://doi.org/10.1142/S0217984916503085>.
- [130] E. N. Lorenz, in *Causes of Climatic Change*, edited by J. M. Mitchell (American Meteorological Society, Boston, 1968) pp. 1–13.
- [131] M. Ghil and A. W. Robertson, *Proc. Natl. Acad. Sci. USA* **99**, (Suppl. 1), 2493 (2002).
- [132] V. Lucarini and A. Gritsun, *Climate Dynamics* **54**, 575 (2020).
- [133] F. Bouchet, J. Laurie, and O. Zaboronski, *Journal of Statistical Physics* **156**, 1066 (2014).
- [134] P. D. Ditlevsen, *Geophysical Research Letters* **26**, 1441 (1999), <https://agupubs.onlinelibrary.wiley.com/doi/pdf/10.1029/1999GL013022>.
- [135] P. Imkeller and I. Pavlyukevich, *Stochastic Processes and their Applications* **116**, 611 (2006).
- [136] A. Debussche, M. Högele, and P. Imkeller, *The Dynamics of Nonlinear Reaction-Diffusion Equations with Small Lévy Noise*, Lecture Notes in Mathematics (Springer International Publishing, 2013).
- [137] F. Yang, Y. Zheng, J. Duan, L. Fu, and S. Wiggins, *Chaos: An Interdisciplinary Journal of Nonlinear Science* **30**, 063125 (2020), <https://doi.org/10.1063/5.0006626>.
- [138] H. Risken, *The Fokker-Planck equation* (Springer, Berlin, 1996).
- [139] G. Margazoglou, V. Lucarini, T. Grafke, and A. Laio, (2020), 10.6084/m9.figshare.13079489.